1-1-2006

# Computational Simulation Of Dynamics Of Nematic Liquid Crystals In The Presence Of Nanoparticles And Biological Macromolecules

Huangli Wu

# COMPUTATIONAL SIMULATION OF DYNAMICS OF NEMATIC LIQUID CRYSTALS IN THE PRESENCE OF NANOPARTICLES AND BIOLOGICAL MACROMOLECULES

By

Huangli Wu

A Thesis
Submitted to the Faculty of
Mississippi State University
in Partial Fulfillment of the Requirements
for the Degree of Master of Science
in Computational Engineering
in the College of Engineering

Mississippi State, Mississippi

August 2006

COMPUTATIONAL SIMULATION OF DYNAMICS OF NEMATIC LIQUID CRYSTALS IN THE PRESENCE OF NANOPARTICLES AND BIOLOGICAL MACROMOLECULES

By

Huangli Wu

Approved:

| | |
|---|---|
| Rajendran Mohanraj<br>Assistant Research Professor of Computational Engineering<br>(Major Professor) | Hyeona Lim<br>Assistant Professor of Mathematics and Statistics<br>(Committee Member) |
| Edward Luke<br>Assistant Professor of Computer Science And Engineering<br>(Committee Member) | Mark Janus<br>Associate Professor of Aerospace Engineering<br>Graduate Coordinator of Computational Engineering |

Roger King
Associate Dean of Research and Graduate Studies of the Bagley College of Engineering

Name: Huangli Wu

Date of Degree: August 5, 2006

Institution: Mississippi State University

Major Field: Computational Engineering

Major Professor: Dr. Rajendran Mohanraj

Title of Study: COMPUTATIONAL SIMULATION OF DYNAMICS OF NEMATIC LIQUID CRYSTALS IN THE PRESENCE OF NANOPARTICLES AND BIOLOGICAL MACROMOLECULES

Pages in Study: 75

Candidate for Degree of Master of Science

Recent research shows that liquid crystals can be used to report the presence of different types of substances through optical amplication of ligand-receptor binding. In this work, simulations based on a coarse-grained method have been performed to study a class of liquid-crystal-based sensors. A tensor order parameter was used to model the liquid crystalline system and the Beris-Edwards formulation was employed to obtain the time evolution of a liquid crystal medium containing particles. The simulation cases are built using three-dimensional unstructured meshes and the simulation geometries studied include simple models involving spheres as well as detailed modeling for a protein. The dynamics of a liquid crystal medium confined between two solid walls has been studied in the presence of spherical particles and a representative biological macromolecule. Comparisons of steady state and transient solutions from the present study with corre-

sponding results from molecular dynamics based simulations in the literature yield good agreements.

# DEDICATION

To my parents and brother.

# ACKNOWLEDGMENTS

I would like to express my sincere gratitude to my major professor, Dr. Rajendran Mohanraj for his endless patient guidance and invaluable feedback. I am also grateful to Dr. Edward Luke and Dr. Hyeona Lim who have served as my committee members and provided helpful advice and Dr. David Thompson who offers me assistantship.

Special thanks to Dr. Edward Luke and Dr. Xiao-Ling Tong, for their help in use of LOCI programming framework, and Paresh Patel for help in performing surface remeshing.

I would like to thank my Parents and the rest of my Family for their support during my work.

Finally, I would like to acknowledge NSF Grant EPS 0132618 for financial support.

# TABLE OF CONTENTS

# LIST OF FIGURES

FIGURE Page

FIGURE Page

# CHAPTER I

# INTRODUCTION

## 1.1 Background and motivation

Current methods used to detect specific chemical compounds such as proteins, viruses and chemicals generally require expensive laboratory-based analytical apparatus (e.g. Gas Chromatography, Mass spectrometry analysis). A new class of sensors based on liquid crystals is a promising alternative. The underlying principle is that liquid crystals (LCs) can be used to amplify and transduce receptor-mediated binding of proteins at surfaces into optical outputs [12]. Optical amplification of binding events at a surface relies on the optical properties of a liquid crystal and its ability to form highly oriented phases [10]. Past experimental studies have shown that the introduction of chemical compounds into uniformly aligned nematic liquid crystals perturbs the local ordering of the LC and is accompanied by the formation of topological defects around these compounds [20]. The important characteristic of such a system is the orientation of the LC at the surface of the substances (e.g. colloidal particles) present in the LC. The effect of this boundary condition imposed at the surface of the particles results in the defect structure in the LC in the vicinity of the particles and this yields a clear optical signal that can be detected visually.

The design of the sensor is based on the sensitivity of the bulk molecular orientation in LC medium to changes at interface boundaries. This type of biosensor essentially consists of a thin film of a nematic LC between two aligning surfaces. In absence of the analyte the sensor is designed to detect, the solid surfaces with appropriate surface treatments impose a uniform state of orientation in the LC medium. When observed through crossed polars, it shows a uniform structure. When the particular analyte of interest is introduced in the LC confined between two walls, the long-range order is destroyed and the occurrence of topological defects gives rise to an optical signature.

The possibility that a particle with homeotropic boundary condition (the liquid crystal molecules are oriented perpendicular to the surface of the particles) may be surrounded by a Saturn ring disclination was first put forward by theoretical studies [15, 25], and then confirmed in experimental observations [11, 18]. It is also possible that a particle is surrounded by a point defect, but the stability of the defect structure depends on many factors including the size of the particles, the strength of the anchoring [21], and the presence of the confining surfaces [10].

Thus the ability of LCs to optically amplify and transduce the binding events at the substrates provides the basis for the design of LC-based bio-sensors. To improve the design for this class of liquid crystal based sensors, a good understanding is required about the occurrence of topological defects and the dynamics associated with them when a certain class of substances is present in a liquid crystal medium. This work will study the

ordering dynamics of a three dimensional nematic film confined between two substrates in the presence of nanoparticles or biological macromolecules.

## 1.2 Literature survey of pertinent experimental and simulation studies

Some work has been done experimentally and computationally for the study of suspension of colloidal particles in nematic liquid crystals. Thermotropic LC was used to detect the binding of analytes with the naked eye [12]. In this experiment, protein Av (avidin) or IgG (Immunoglobulin G) was binded to ligands hosted within a SAM (self assembled monolayer) of molecules supported on a gold film. Liquid crystal cells were formed by separating two SAMs with a spacer of thin plastic film. The adsorbed analytes (Av, IgG) change the orientations of molecules of supported LC, and this gives rise to an optical signature. The results experimentally demonstrate that the liquid crystals can be used to report the ligand-receptor binding at solid surfaces. Recently, numerical simulations have become more common. A molecular dynamics (MD) simulation was used to investigate the topological defects that appear in the liquid crystalline medium around a spherical droplet in two-dimensional systems [2]. This work discusses three possible defect structures in the LC around the particles and their stability under different conditions. Using a description based on the director, the topological defects in the LC around a spherical colloid particle have been studied through the use of Monte-Carlo simulations [21]. The analysis in this study was focused on the effects of anchoring strength of the boundary surfaces. Dynamic field theory with tensor order parameter was used

to compute the evolution of the liquid crystal in the presence of adsorbed nanoparticles within two-dimensional LC system [8, 22]. The effects of the concentration of particles in the LC were analyzed in this study. Monte Carlo simulations and dynamic field theory were used to study the defect structure for suspended particles in the LC and their interactions [10] in two-dimensional system. Comparison between these two methods shows good quantitative agreement. Adaptive mesh refinement scheme in two-dimensional system was implemented to detect the defect structure of a nematic liquid crystal around a spherical particle [6]. With this method, the resolution can be made fine enough in the regions of interest with significant change in the orientation of the directors.

### 1.3 Simulation with tensor order parameter

A description limited to specifying a single scalar order parameter for the whole liquid crystal medium is inadequate for the present study. Accurate description of the dynamics associated with the defects in the liquid crystal medium in the presence of nanoparticles or biological macromolecules requires a specification in terms of the tensor order parameter. In this work, we use dynamic field theory (DyFT) of the tensor order parameter to study the dynamics of LCs in the presence of the particles. The tensor order parameter formulation includes both long-range and short-range order elastic effects that govern LC dynamics in contrast to classical theories, which consider one effect only. It has been successfully applied to the study of defect structures around the particles in LCs [24]. The length scales of interests for the nanoparticles, which denote a substance characterized by

nanoscopic dimensions (e.g. colloidal particles), and macromolecules are in the order of nm to microns.

From section 1.2, we know in some studies two-dimensional system was implemented. In some studies, a numerical analysis based on an adaptive grid has been used to study the director configuration around the spherical particles. In the present study, we provide the results based on three-dimensional simulation using an unstructured mesh. This method provides significant leeway in using high resolution in regions of interests such as the locations where the defects are expected to be located and low resolution in other regions. This enables us to perform efficient computations and present a complete description of the director fields.

### 1.4 Objective and scope of the present study

The objective of the present study is to develop and demonstrate a simulation platform for modeling the liquid crystal sensor. This simulation platform will (a) use a description based on the tensor order parameter for the liquid crystal, (b) have the ability to handle complex geometry using three-dimensional unstructured meshes to model biological macromolecules, and, (c) be suitable for performing large computations on a parallel computing framework.

In this work, we will study a simulation framework that uses a tensor order parameter based approach for modeling the behavior of this class of liquid-crystal-based sensor. From this system, the ordering dynamics for liquid crystals confined between two solid

walls in the presence of particles has been studied. The size of the particles is of the order of tens or hundreds of nanometers. This is close to the range of sizes for the target substances that are to be detected by the experimental sensors. The relaxation of the nematic is described by a time evolution equation for the tensor order parameter using Beris-Edwards formulation and this includes both short-range and long-range order elastic effects.

The simulation results presented in this study include the following:

1. The defect structure for one spherical particle immersed in a nematic host.
2. Dynamic interaction between one spherical particle and disclination lines in the LC.
3. Interactions between two spherical particles immersed in the LC.
4. The dynamics in LCs when the spherical particles are adsorbed on the solid surfaces.
5. The defect structure for a case involving a biological macromolecule with detailed representation of its three-dimensional geometry.

The remainder of this thesis is organized as follows. Chapter II gives the basics for the properties of liquid crystals. In Chapter III we present the computational details and the model we used to simulate the liquid crystal medium in the presence of the particles. Chapter IV contains the results of the simulations. Concluding remarks and suggestions for future work are given in Chapter V.

# CHAPTER II

# LIQUID CRYSTAL BASICS

This chapter deals with the basic concepts of liquid crystals and discusses topics such as the measure of the orientational order for liquid crystal, the accompanied defect structure, and applications of liquid crystals. Most of the discussion is based on the contents in Refs. [4, 19].

## 2.1 What are liquid crystals?

There are three common states of matter in the world including solid, liquid and gas. The differences among them are the degree of order including positional order and orientational order.

In the solid state, the molecules are constrained to occupy only certain positions. We call this condition as positional order. In addition, the molecules in these specific positions are arranged in a fixed orientation. When a solid melts to a liquid, both types of order are lost completely. The molecules in liquid phase can move and tumble randomly. In this state, the intermolecular attractive forces that kept a solid together are now only strong enough to keep the liquid molecules close together. When a liquid becomes gas, the random motion the molecules have is increased to overcome the intermolecular forces and the molecules finally spread out to fill any container that holds them.

An important property that plays a role in distinguishing between the three states of matter is temperature, which is a measure of the extent of molecular motion. The higher the temperature, the lower the extent of order. By increasing the temperature, any solid can be converted to a liquid and later to a gas.

A liquid crystalline phase occurs in some substances and in this state the substance has some properties of both liquids and solids. Figure 2.1 shows the order in solid, liquid and liquid crystal.

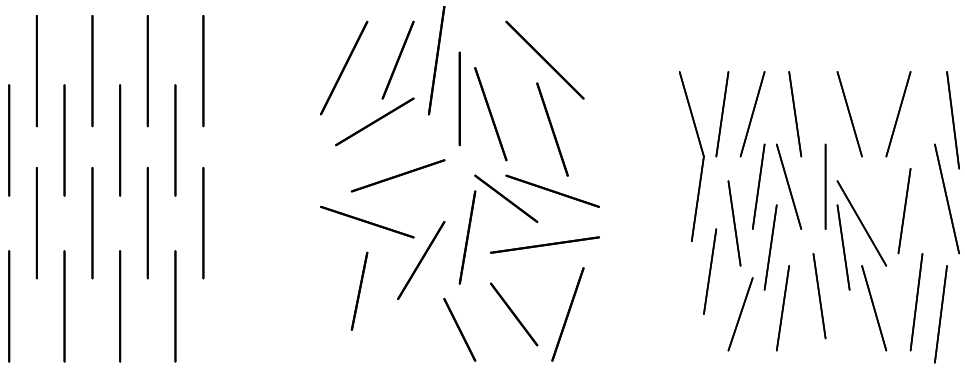

Cyrstalline Solid Liquid Liquid Crystal

Figure 2.1

Schematic representation of molecular order in a crystalline solid, regular isotropic liquid and liquid crystal

## 2.2 Liquid crystal order

In liquid crystal, the orientational order is not nearly as perfect as in a solid. We can define a unit vector $n$ called the director to be the average molecular orientation direction.

The director is a variable, which is dependent on both space and time coordinates and it is denoted by $n(x,t)$. Each molecule makes an angle with the director denoted by $\theta$ (Figure 2.2), which we can measure. The average angle could then be computed as a measure of the amount of orientational order denoted by $S$ (Eqn. (2.1)), which describes the degree of order.

$$S = average\ of\ (\frac{3}{2}cos^2\theta - \frac{1}{2}) \tag{2.1}$$

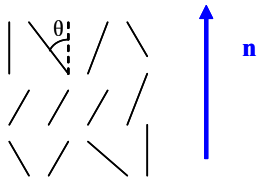


Figure 2.2

$\theta$ denotes the angle between a molecule and the director $n$

Normally in the equilibrium liquid crystal state the range of the scalar order parameter is given by $0 < S < 1$. With the change of the temperature, the material will change from $S = 1$ in the crystalline state to $S = 0$ in the isotropic state at high temperature.

### 2.3 Biaxial liquid crystals

In a biaxial system there is no axis of complete rotational symmetry. Hence there is no axis such that rotation through an arbitrary angle about that axis leaves the system

unchanged. The liquid crystal can be biaxial. Therefore to define the state of orientation of the liquid crystal, two perpendicular axes, $n$ and $m$ are required. The third one can be specified as perpendicular to the other two. Two directors and the corresponding two scalar order parameters can then be defined. Thus the liquid crystals with biaxial state can be described by two director variables $n$ and $m$ (Figure 2.3) and two scalar order parameters, $S_1$ and $S_2$.

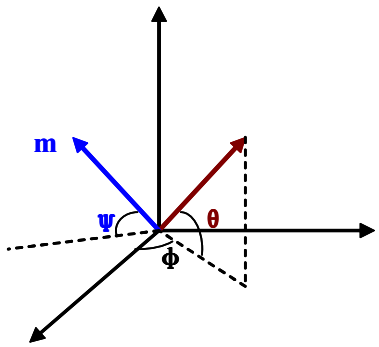


Figure 2.3

The directors $n$ and $m$ in terms of Euler angles $\theta$, $\varphi$ and $\psi$

From Figure 2.3, we can write director $n$ as the following:

$$n = (cos\theta * cos\varphi, cos\theta * sin\varphi, sin\theta) \tag{2.2}$$

The director $m$ is perpendicular to $n$, we can write $m$ as the following:

$$m = (sin\varphi * cos\psi - cos\varphi * sin\psi * sin\theta, -sin\varphi sin\psi * sine\theta - cos\varphi * cos\psi, sin\psi * cos\theta) \tag{2.3}$$

From Equations (2.2) and (2.3), the liquid crystal system could be described using five independent variables including $\theta$, $\varphi$, $\psi$, $S_1$, $S_2$, which constitute the basis for tensor order parameter theory.

## 2.4 Tensor order parameter $Q$

From the previous section, we know that the liquid crystal system can be described by five independent variables. A 3*3 matrix can be constructed, which contains the information for these five variables. The 3*3 matrix can be written in the following form:

$$M = S_1(n * n) + S_2(m * m) \tag{2.4}$$

where $n$, $m$ are vectors of directors, $ij^th$ element of the product $n * n$ is $n_i n_j$. The matrix form for $M$:

$$M = \begin{bmatrix} m_1 & m_2 & m_3 \\ m_2 & m_4 & m_5 \\ m_3 & m_5 & (S_1 + S_2) - m_1 - m_4 \end{bmatrix} \tag{2.5}$$

The tensor $Q$ can then be defined as

$$Q = S_1(n * n) + S_2(m * m) - 1/3(S_1 + S_2)I \tag{2.6}$$

where $I$ is the identity matrix. Note that the above definition for $Q$ is such that the trace of $Q$ is zero. The tensor $Q$ can be written as a symmetric traceless matrix.

$$Q = \begin{bmatrix} q_1 & q_2 & q_3 \\ q_2 & q_4 & q_5 \\ q_3 & q_5 & -q_1 - q_4 \end{bmatrix} \tag{2.7}$$

The $Q$ tensor theory is used in our work to investigate the dynamics of LCs in the presence of nanoparticles and biological macromolecules.

## 2.5 Defect structure in liquid crystals

In previous sections, we have given the definition for the director at a point, which is the direction of preferred orientation of the molecules in the neighborhood of that point. Defect could be defined as the region where the director changes abruptly. There are several types of defects. In this work, we study two of them. The first is a point defect called a dipolar or satellite defect. The second is a quadrupolar or Saturn ring defect (Figure 2.4).

An abrupt change in the direction of preferred orientation always implies severe distortion of the director configuration in the vicinity of the defect. The homeotropic anchoring at the surface of the particles (the liquid crystal molecules are oriented perpendicular to the surface of the particles) creates a topological mismatch of the director field between the director on the particle surface, which generates the defects around the particles in LCs,

and the uniform director at large distances. The structure of defects plays an important role in the optical characteristics of the LC based sensors investigated in the present study.

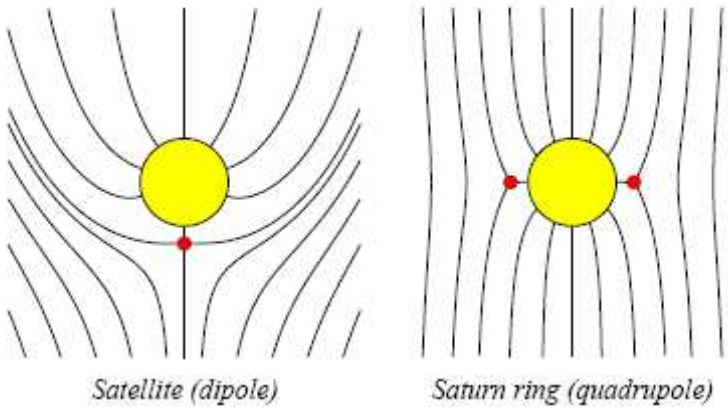


Figure 2.4

Sketches of the satellite defect and Saturn-ring defect (reproduce from [2]).

## 2.6 Coarse-grained method

The state of a liquid crystal system can be specified using a microscopic description involving the orientation of individual molecules. This approach limits the size of the system that can be simulated. In contrast, in a coarse-grained framework, the state of the system at a point in space and time is defined based on the average orientation of a large number of molecules. The spatial resolution associated with this meso scale, coarse-grained model is of the order of a few nanometers or larger. A coarse grained description, such as the one used in the Q-tensor based model of this study, enables simulation of

phenomena encompassing large length and time scales compared to a detailed molecular description.

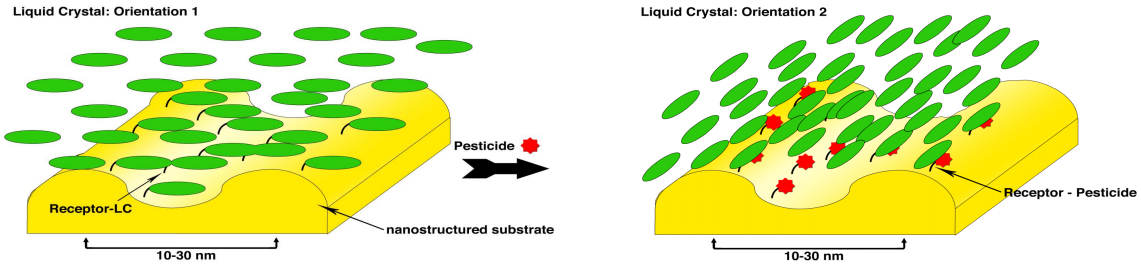


LC orientation in the absence of analyte

LC orientation in the presence of analyte (pesticide)

Figure 2.5

LC sensor schematic

## 2.7 Applications of liquid crystals

The most common application of liquid crystalline substances is in display devices (LCD, liquid crystal display). Other applications include temperature measurements and optical imaging. Recently, its application in bio-sensor has attracted wide interest [8, 10]. In display devices, the liquid crystal orientation is determined by the applied electric field. However, for the sensor system in the present study, the orientation of the liquid crystal is influenced by the concentration of a specific analyte (target compound that needs to be detected). The use of a liquid crystal film adjacent to a surface involving nanoscale corrugations can enable detection of different biological substances (e.g. proteins, viruses).

Operating Principle: The LC based sensor is designed such that the binding between the receptor and the targeted analyte is energetically more favorable compared to the receptor-LC binding. Hence, introduction of the analyte forces the liquid crystal to assume a new orientation, which is determined in part by the nanostructured surface, and this change in orientation can be easily visualized (Figure 2.5).

Some of the advantages of this class of sensors are as follows:

1. This simple, cost-effective, portable sensor platform is a promising alternative to present methods that require expensive lab-based instrumentation and highly trained personnel.
2. Attaining high sensitivity (detection of few parts per billion) and selectivity (ability to distinguish between similar compounds) is feasible.
3. The chosen liquid crystal based sensor platform, which utilizes recent advances in fabrication of nanostructured surfaces, has been demonstrated to detect a wide range of substances including organophosphates (pesticides & nerve gases are organophosphates), proteins and viruses.

# CHAPTER III

# SIMULATION METHODS

## 3.1 Three-dimensional model of the sensor used in simulation

We consider a model for the sensor in which nanoparticles or biological macromolecules are suspended in a nematic liquid crystal medium confined between two parallel surfaces. This mimics the geometry of the LC based sensors in the experiments. Figures 3.1 (a) and (b) show sensor model containing spherical particles, and a detailed geometry for a biological macromolecule, respectively.

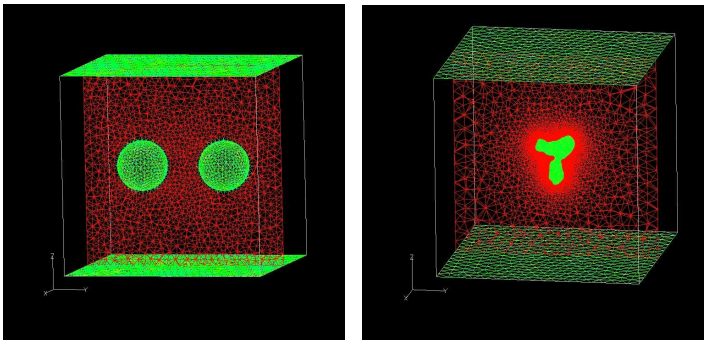

(a) (b)

Figure 3.1

Schematic view of a model LC sensor: (a) the nanoparticles are modeled as spherical particles; (b) a biological macromolecule is specified using detailed geometry. Surface meshes for the top and bottom boundaries are also shown

In the absence of particles, long-range uniform orientation occurs throughout the liquid crystal film. When the analyte of interest (e.g. a protein or a virus) is bound to the interface boundary, this can destroy the long-range order through the occurrence of topological defects and facilitate optical detection. The director description is often used to describe the structure of the nematic liquid crystal at micrometer length scales around the particles. However, in the design of optical biosensors, the typical targets for the biosensors such as proteins have sizes on the order of 10 to 100 nanometers. In addition, the director description is not appropriate for study of the region close to the core defect, where the average molecular orientation changes abruptly. A better approach towards description of the defect of structure of the core defect relies on the tensor parameter [8]. It also provides an accurate representation of the structure of defects and director down to length scales of a few molecular diameters [8, 14, 22]. Therefore coarse-grained method in terms of tensor order parameter based on a dynamical field theory is used to track the dynamics of the LC and the immersed particle is treated as a solid object [13]. The tensor order parameter (details discussed in section 2.4) is a symmetric traceless matrix $Q_{ij} =< u_i u_j - 1/3\delta_{ij} >$ which contains all the information about the nematic state of LCs and can be written as given in Eqn. (2.7). The brackets $< A >= \int A\psi(u)du, (A = u_i u_j - 1/3\delta_{ij})$ denote an average over all possible orientations on the unit sphere. The tensor $Q(r)$ defines a coarse-grained order parameter that represents the local average at point $r$. It includes five independent variables. The optical signature of the system depends upon the relaxation of the LC after the particles get adsorbed at the interface boundaries. This relaxation

process of the liquid crystal could be described by an unsteady partial differential equation for the tensor order parameter that includes both short-range and long-range order elastic effects. The equilibrium properties of the LC could be described by Landau-De Gennes free energy [5].

The Beris-Edwards formulation [3] was employed here to obtain the time evolution of the coarse-grained tensor order parameter. The formulation is:

$$\frac{\partial Q}{\partial t} = \Gamma \left[ -\frac{\partial F}{\partial Q} + \frac{1}{3} Tr(\frac{\partial F}{\partial Q}) I \right] \tag{3.1}$$

The coefficient $\Gamma$ is given by $\Gamma = 6D^* / \left[1 - 3Tr(Q^2)\right]^2$, where $D^*$ is the rotational diffusion coefficient for the LC. The free energy $F$ of the LC includes two contributions, the long-range and the short-range interaction contributions, which can be de described as follows:

$$F = \int_v F_s + F_e dr \tag{3.2}$$

The long-range contribution is of the form:

$$F_e = \int dr \frac{L_1}{2} (\partial_\alpha Q_{\beta\gamma})^2 \tag{3.3}$$

where $L_1$ is a material-specific elastic constant. A short-range elastic contribution of the form:

$$F_s = \int dr \left\{ \frac{A}{2} \left( (1 - \frac{U}{3}) Q_{\alpha\beta} Q_{\alpha\beta} - \frac{AU}{3} Q_{v\gamma} Q_{v\alpha} Q_{\alpha\gamma} + \frac{AU}{4} (Q_{\alpha\beta} Q_{\alpha\beta})^2 \right) \right\} \tag{3.4}$$

The parameter $A$ is to control the relative magnitude of the two contributions. The relative magnitude between two contributions Eqn. (3.3) and Eqn. (3.4), depends on the liquid

crystal of interest. For low molecular weight LCs, long-range interactions are dominant, while for polymetric LCs, short-range interactions are dominant. $U$ is the dimensionless nematic potential strength. The characteristic length could be defined as $\xi = \sqrt{18L_1/AU}$ and it provides a characteristic length scale for changes of the order parameter. At the isotropic-nematic first-order transition, $\xi$ is about several molecular lengths, with $\xi$ 20nm [16]. The characteristic time scale can be defined as $\tau_0 = |6DA(1 - U/3)|^{-1}$ [16]. From equations (3.1) to (3.4) we can obtain the following equation:

$$\frac{\partial Q}{\partial t} = -\frac{6D}{(1 - 3(Q:Q)/2)^2}$$

$$\{A(1 - \frac{U}{3})Q - AU[Q \bullet Q - \frac{1}{3}(Q:Q)\delta] + AU(Q:Q)Q - L_1\nabla^2 Q\} \tag{3.5}$$

The quantity $Q$ should satisfy the traceless condition $Tr(Q) = 0$. The eigenvalues of the matrix $Q$ are described by the following diagonal matrix:

$$\begin{bmatrix} \lambda_1 & 0 & 0 \\ 0 & \lambda_2 & 0 \\ 0 & 0 & \lambda_3 \end{bmatrix} = \begin{bmatrix} \frac{2S}{3} & 0 & 0 \\ 0 & \frac{S_b - S}{3} & 0 \\ 0 & 0 & -\frac{S_b + S}{3} \end{bmatrix} \tag{3.6}$$

where $S$ denotes the nematic scalar order parameter and $S_b$ denotes the biaxiality. The choice for the ordering of the eigenvalues is such that $\lambda_1 \geq \lambda_2 \geq \lambda_3$. We can obtain the following:

$$S = 3/2\lambda_1 \tag{3.7}$$

$$S_b = 3/2\lambda_1 + 3\lambda_2 \tag{3.8}$$

The eigenvector associated with the highest eigenvalue $\lambda_1 = 2S/3$ corresponds to the generalization of the director $n$. At the bounding surfaces, we assume $Q$ to be uniaxial and of the form

$$Q = S^{eq}(nn - \delta/3) \tag{3.9}$$

where $n$ is the preferred orientation of the strong anchoring at the surfaces. The equilibrium scalar order parameter $S^{eq}$ is obtained from the Doi theory [19].

$$S^{eq} = (1 + 3\sqrt{1 - 8/3U})/4 \tag{3.10}$$

The choice for the orientation of the coordinate system is such that the two parallel boundary surfaces that represent the interface boundaries for the LC medium (the top & bottom surfaces for which surface meshes are shown in Figure 3.1) are perpendicular to the $z$ direction ($z$ axis is along vertical direction). The director is specified along a particular orientation (this can be parallel or perpendicular to the interface boundary surface) at the interface boundary. Periodic boundary conditions are imposed in the $x$ and $y$ directions. We consider the case of strong homeotropic anchoring (i.e. LC orientation at the boundary of the nanoparticle or biological macromolecule is along the unit vector normal to the surface). For the initial conditions, the nematic scalar order parameter is set to the equilibrium value $S^{eq}$ (see Eqn. (3.10)) throughout the domain and the corresponding initial tensor $Q$ in the simulation box is assumed to be uniaxial and is given by:

$$Q = S^{eq}(nn - \delta/3) \tag{3.11}$$

The time evolution of the state of the liquid crystal medium is obtained by the numerical solution of Eqn. (3.5) using an explicit, cell-centered, finite volume scheme with a second order Runge-Kutta scheme for time integration. The implementation of the numerical solution is through a rule-based framework (LOCI framework [17]) that is well suited for efficient solution of continuum models in large scale parallel computing clusters.

Once the solution for tensor order parameter $Q$ is given at a particular location, by calculating its eigenvalues and eigenvectors, the local state of the LC could be described in terms of the scalar order parameter $S$ (Eqn. (3.7)), biaxiality $S_b$ (Eqn. (3.8)) and director orientation (the eigenvector corresponding to the maximum eigenvalue $\lambda_1$).

The system evolves starting from the specified initial configuration and attains a steady state in the final equilibrium configuration. One choice for the initial condition is specifying the values for the $Q$ tensor corresponding to a uniaxial state with uniform orientation of the corresponding director in a specified direction throughout the computational domain. Changes in initial conditions in this work are introduced through fluctuations in the orientation of the director of different strength or magnitude. A parameter $\epsilon$ is introduced such that when it is zero, this corresponds to uniform orientation of the director everywhere in the liquid crystal medium and when the parameter is 1.0, this corresponds to totally random orientation in the different cells. It was observed that $\epsilon$ had an effect on convergence and that when $\epsilon$ increases beyond a certain value, convergence of the simulations to a steady state stalls. It has been verified that for different choices of the parameter $\epsilon$ (typically with $\epsilon \leq 0.5$), the same converged steady state solutions are obtained. For this work

simulations have been performed with at least two different values of $\epsilon$ and essentially the same results have been obtained. Such simulations are used to account for variations in initial conditions.

The convergence to steady state can be monitored based on the change in the residual in the numerical computations. As the residual a quantity that numerically drives the change in $Q$ with time in the numerical solution procedure decreases continuously, convergence towards a steady state solution is obtained. Sufficient number of time steps have been used to ensure that the obtained solution is well converged. The total number of time steps used in different cases to ensure convergence is of the order of $10^5$. Most of the changes occur during the earlier portion of the simulation duration and the rate of decrease of the residual is much smaller towards the end, as expected. Depending on the size of the system and time required for convergence simulations have been performed using different number of processors (e.g. 4 to 64 processors).

### 3.2 Parameters for the simulations

In this work, a set of parameters was chosen to represent a low molecular weight LC, which corresponds to the physical properties of $5CB : A = 1, L_1 = 0.55, D^* = 0.35, \ and \ U = 6$. The corresponding scalar order parameter $S^{eq} = 0.81$ . The characteristic length scale for variation of properties in the liquid crystal given by $\xi = \sqrt{18L_1/AU} = 0.856$ accordingly. The characteristic time in this work, which is defined as $\tau_0 = |6DA(1 - U/3)|^{-1}$, is of the order of 100 ns. Three-dimensional unstructured

meshes are used to describe the region occupied by the liquid crystal medium surrounding the spherical regions that model the biological molecules.

# CHAPTER IV

# RESULTS AND DISCUSSION

This chapter presents results obtained from simulations using several examples. Substances contained within the LC medium have been modeled as spherical particles representing nanoparticles in several examples. However cases that contain detailed geometric modeling for a biological macromolecule have also been included.

## 4.1 Defect structures around one spherical particle

To understand the interaction between the particles, it is important to know the liquid crystal ordering near one isolated particle. In this section, we will study the dynamics of a liquid crystal around one spherical particle including the topological defects around the particle, the change from satellite defect to Saturn ring defect, and the influence of the size of the particle upon the satellite defect. This will provide us with a general understanding of the defect structure for one particle in a LC medium.

### *4.1.1 Topological defects around one particle*

This example shows the simulation results for one spherical particle immersed in the LC in steady state. The outer boundary corresponds to a cubic domain of length of 6 units. The radius of the sphere is 1 unit. The director is initially aligned along the $x$ direction with

$n = (1, 0, 0)$. The chosen mesh contains 170,623 computational volume elements. After 220,000 computational time steps, the system is very well converged to a steady state. The results were analyzed to obtain scalar order parameters (Figure 4.1), the biaxiality map (Figure 4.2), director (Figure 4.3), director streamlines (Figure 4.4), order parameter with streamline (Figure 4.5), and iso-surface for scalar order parameter (Figure 4.6).

From these images, we can observe that in the steady state solution a Saturn ring defect is formed close to the sphere (Figure 4.1 & 4.6) and is located on the equatorial $y - z$ plane. From the director orientation (Figure 4.3) and also through the director streamline image (Figure 4.4), it is seen that for regions far away from the sphere, the director orientation is approximately uniform and is along the x-axis. This indicates that the ring defect does not force long-range distortions in the director field. Its core region is located very close to the sphere's surface and the director distortion disappears quickly in the bulk of the LC. This is in agreement with the quadrupolar nature of the defect: far from the particle the director deviation angle has asymptotic behavior $\beta\ (R/r)^3 sin2\theta$ (refer to Figure 4.7 for the definition of $\beta, r, \theta$; $R$ is the radius of the sphere and $r$ is the radial coordinate in the spherical coordinate system) [2]. Figure 4.2 depicts contour plots for the biaxiality parameter and shows that the liquid crystal in the region close to the sphere, and near the defect core, is strongly biaxial, and in the area far away from the sphere, it is uniaxial. Comparison of figures 4.1 and 4.4 shows the relationship between the scalar order parameter and the director. The scalar order parameter attains the minimum value in the region where the director changes abruptly. Comparing figures 4.1 and 4.2, we see that

the region where the order parameter $S$ has the minimum value is also the region where the biaxiality has the maximum value.

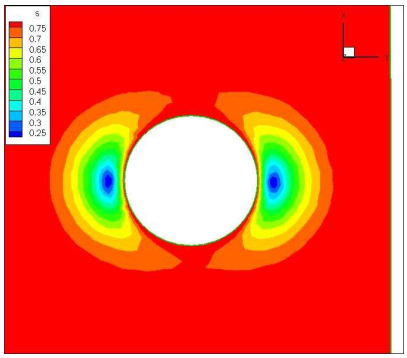


Figure 4.1

Scalar order parameter contour in $x - y$ plane with $z = 0$

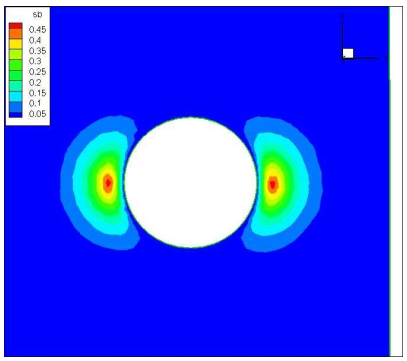


Figure 4.2

Biaxiality contour in $x - y$ plane with $z = 0$

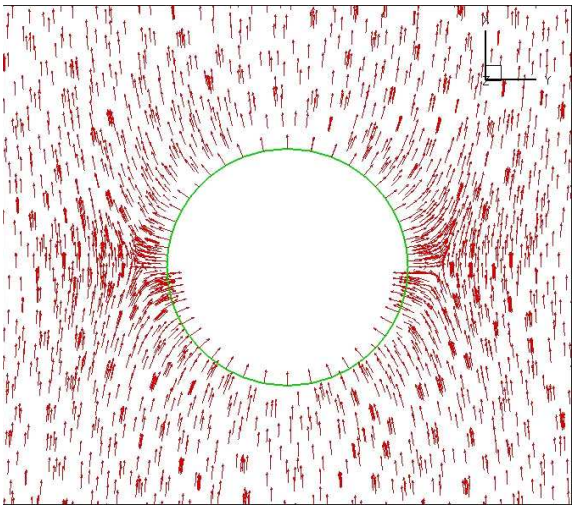

Figure 4.3

Director map in $x - y$ plane with $z = 0$

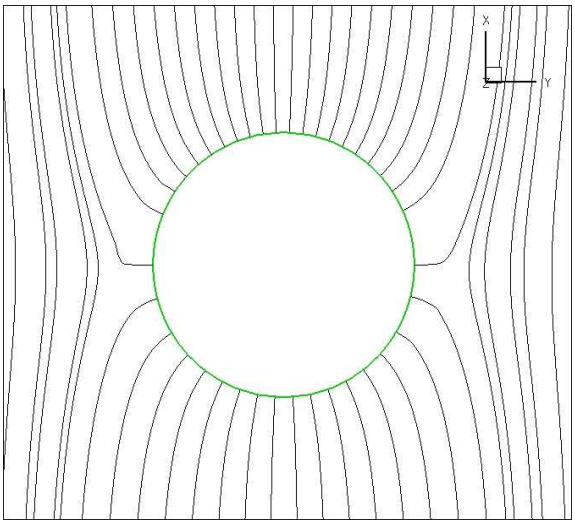

Figure 4.4

Director order streamlines $x - y$ plane with $z = 0$

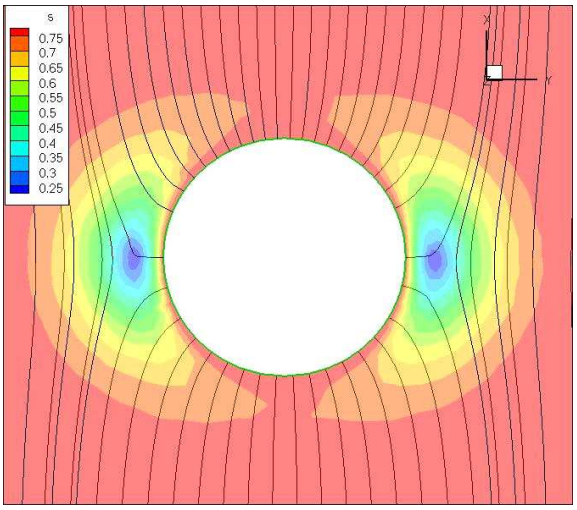


Figure 4.5

Order parameter map with director streamlines in $x - y$ plane with $z = 0$

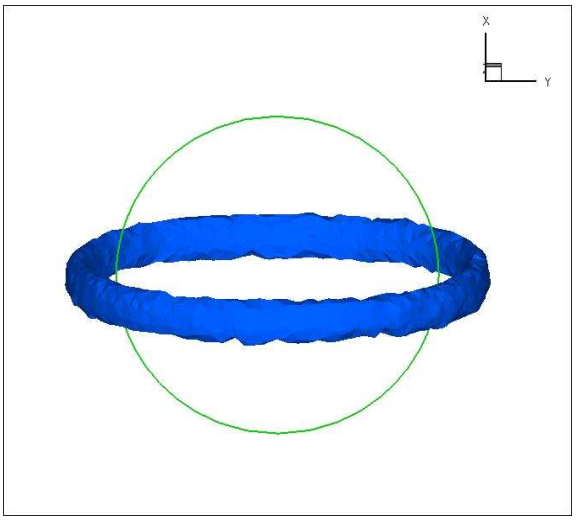


Figure 4.6

Iso surface for scalar order parameter when $S = 0.28$

Parameter profiles and biaxiality profiles along the radial direction are shown in figures 4.8 and 4.9. The shape of these profiles in general reflects the typical structure of the core: the center of the core has lower order than the bulk and the core region extends over a few molecular lengths [2]. As mentioned before, using order parameter profiles one can define the position of the Saturn ring as the location of the minimum of the scalar order parameter. It also can be defined as the location of the maximum of the biaxiality (refer to figures 4.1 & 4.2). From the order parameter and biaxiality parameter profiles, we can see that the defect core is located at about $(r - R) \approx 0.25$. In this case, the radius of the sphere is 1 unit. The ring defect radius $a_r \approx 1.25$ and then the ratio $(a_r - R)/R \approx 0.25$. This is in good agreement with the theoretical results for which the corresponding ratio is about 0.25 [15]. The dependence of this ratio upon other parameters will be discussed later.

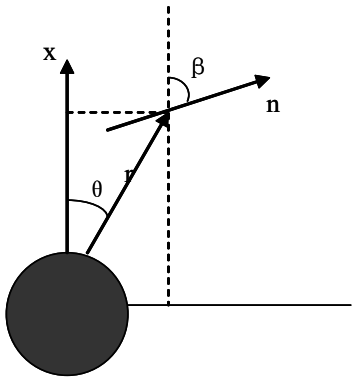


Figure 4.7

Coordinate system and definitions for different symbols for a case containing a single spherical particle

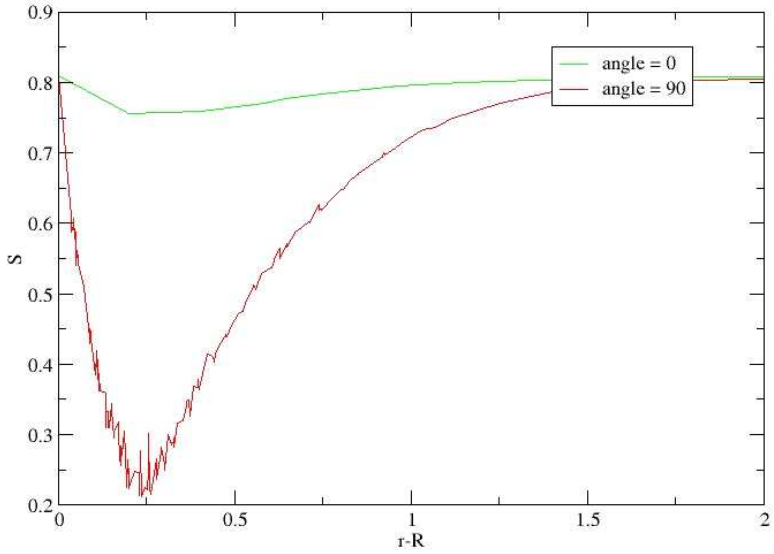


Figure 4.8

Scalar order parameter profiles for the ring defect along the directions $\theta = 0, \pi/2$ ($\theta$ has the same definition as in Figure 4.7). The minimum of the order parameter defines the position of the disclination core. $R$ is the radius of the sphere. $r$ is the distance from the center of the sphere

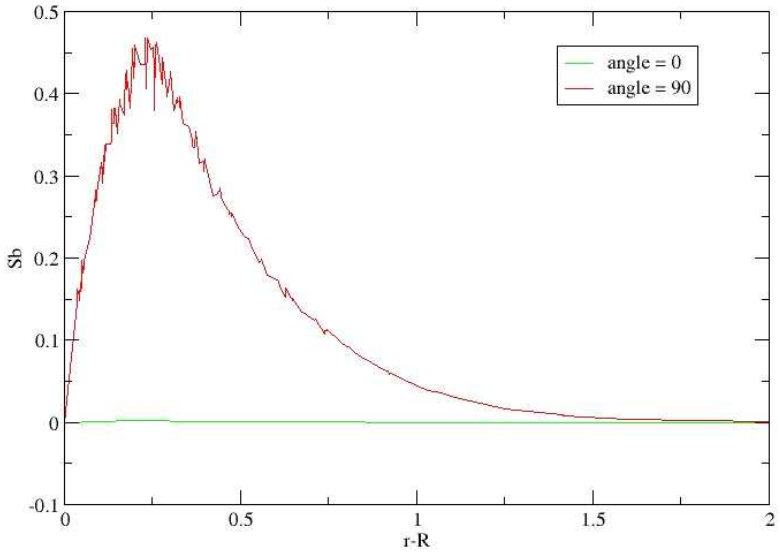


Figure 4.9

Biaxiality profiles along the direction $\theta = 0, \pi/2$. The peak of the biaxiality is centered on the defect core and coincides with the minimum of the order parameter in Figure 4.8. $R$ is the radius of the sphere. $r$ is the distance from the center of the sphere

### *4.1.2 Evolution of the defect structure*

In this section, we will study how an initial configuration corresponding to a satellite defect in the vicinity of a colloidal particle evolves in time and results in a saturn ring type defect. In this case, one spherical particle was centered in the cubic domain with 4 units length. The radius of the particle is 0.2 units. The mesh has 72,000 volume elements. The initial condition for the director is specified in terms of an approximate analytical function [2] in the following form:

$$\begin{aligned} &\beta(r,\theta) = \theta - arctan\tfrac{sin\theta}{1/f(r)+cos\theta} \\ &1/f(\infty) = 0 \\ &f(a_s) = 1 \end{aligned} \tag{4.1}$$

$a_s$ is the distance between the defect core and center of the sphere. In this case $a_s \approx 1.4R$ (variables $\beta$, $\theta$, $r$ are defined in Figure 4.7). $f(r)$ is supposed to be a unique function of $r$ which does not depend on the angle $\theta$.

Figures 4.10 - 4.12 show the variation in the scalar order parameter and the director streamlines in the $x-y$ plane for the initial, intermediate and final states. Because of the resolution limitation, the defect structure is not symmetric about a vertical axis but the resolution is adequate for observing the expected transient and converged solution patterns. From these images, we can observe the transition process from satellite defect to Saturn ring structure. The initial structure corresponds to a satellite defect (Figure 4.10). After about 30,000 computational time steps, this becomes an off-center Saturn ring (i.e. the center of the Saturn ring does not coincide with center of the spherical particle, see

Figure 4.11). This off-center ring gradually approaches the equatorial plane and at around 200,000 computational time steps, the converged structure corresponding to a Saturn ring (this is not off-center) around the particle (Figure 4.12) is obtained.

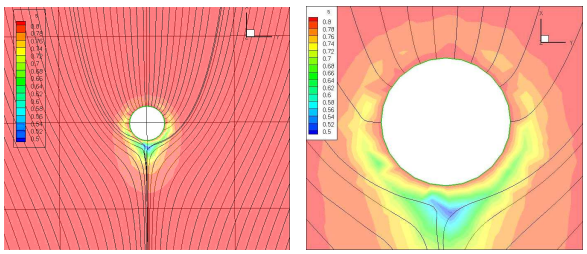

(a) (b)

Figure 4.10

Director and scalar order parameter map of the satellite defect in $x - y$ plane with $z = 0$. (b) is a magnified view of the region close to the sphere

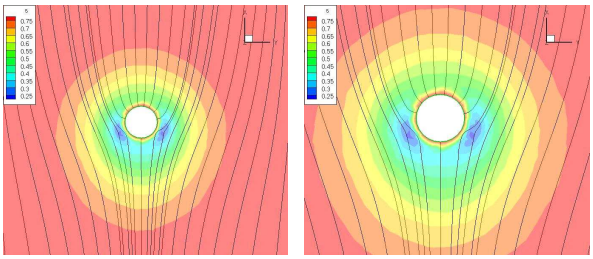

(a) (b)

Figure 4.11

Director and scalar order parameter map for the off-center ring configuration in $x - y$ plane with $z = 0$. (b) is a magnified view of the region close to the sphere

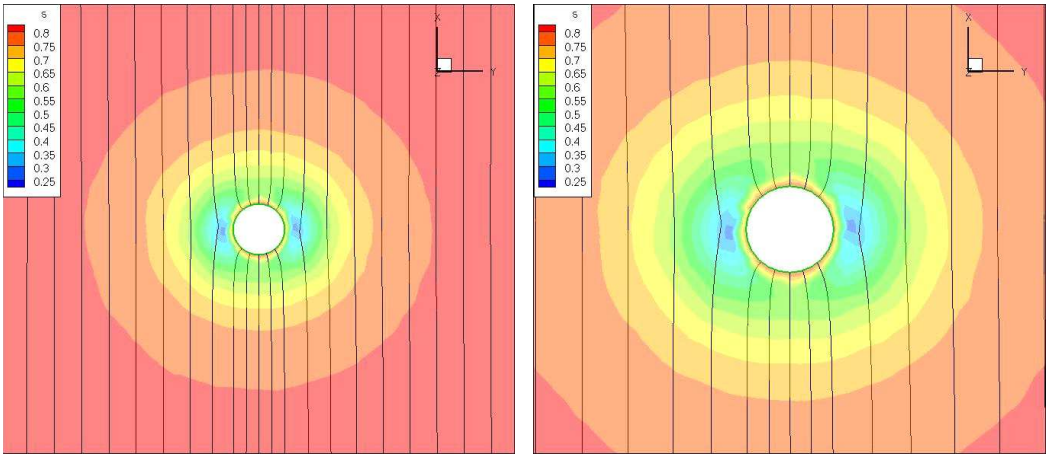


(a) (b)

Figure 4.12

Director and scalar order parameter map for the saturn ring defect in $x - y$ plane with $z = 0$. (b) is a magnified view of the region close to the sphere

Unlike some continuum approaches for solution of liquid crystal orientation involving minimization of energy through an optimization procedure, the present approach involves obtaining a time accurate solution for the evolution of the system. For this approach, in addition to the converged steady state solution, which corresponds to a minimum energy configuration, one also obtains intermediate states during the evolution of this system and these are of physical significance. The system finally converges with a Saturn ring defect. This is in accordance with the results observed in another study that uses detailed molecular dynamics based simulations [2] (see Figure 4.13). In that study, it is shown that under certain conditions, an initial configuration corresponding to a satellite type defect

(Figure 4.13.(a)) in the vicinity of a colloidal particle evolves in time, becomes off-center ring (Figure 4.13.(b)), and finally results in a Saturn ring type defect (Figure 4.13.(c)).

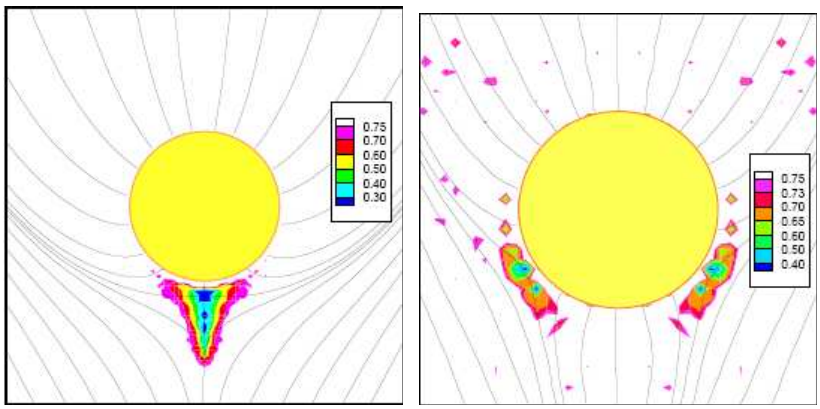


(a) (b)

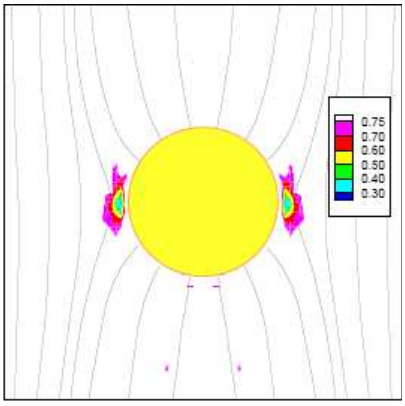


(c)

Figure 4.13

Director map of: (a) satellite defect; (b) off-center ring defect; (c) Saturn ring defect; Radius of sphere equals 15 units. (These results are reproduced from [2] and were obtained using MD simulations.)

From the previous section, we know that the final configuration is a Saturn ring structure. It seems that the Saturn ring is a stable configuration compared with satellite defect and off-center ring. However, it is true only if the size of the particle is very small. In chapter III we have mentioned the characteristic length in our simulation is about 0.856. One unit of length is about 20nm. Thus in this case, the radius $r$ = 0.2 which corresponds to about 4.7nm. In the previous case, $r$ = 1 which corresponds to about 23.5nm. The Frank theory predicts that the Saturn ring loses stability at $R$ = 720nm [26 - 27]. Thus under $R$ = 720nm, Saturn ring is stable. When $R > 720$nm, then independent of the initial condition, the final solution should correspond to satellite defect. Since verifying this requires use of a particle size that is significantly large and requires a large amount of computational time, this verification has not been included in this study.

### *4.1.3 Effect of particle size*

In section 4.1.1, it was mentioned that the ratio $(r - R)/R$ is not fixed. This ratio depends on the radius of the sphere ($r$ here points to the distance from the core defect to the center of the sphere; $R$ is the radius of the sphere). Simulations have been performed for several sizes of the spheres and figures 4.14 - 4.17 show the variation of the scalar order parameter along $y$ direction. For cases with $R$ = 0.2, 0.5, 1.0 and 6.0, the ratio $(r - R)/R$ is about 0.35, 0.3, 0.25. and 0.15, respectively. The bigger the radius, the lower the value of the ratio $(r - R)/R$ is. This may be due to the fact that the energy associated with the Saturn ring defect increases when the length of the Saturn ring increases. In

three dimensions, the 'line tension' associated with the Saturn ring defect has the effect of reducing the length of the disclination [21].

### 4.2 Annihilation of two disclination lines

In this section, we will study how one spherical particle accompanied by its topological defects interacts with neighboring disclination lines. Simulation results for this problem are available from another study [9] for comparison. Initially, the director profile $(n_x, n_y, n_z) = (cos\phi, 0, sin\phi)$ is given by the superposition of two disclination lines of opposite charge, and $\phi$ is given as follows:

$$\phi = -\frac{1}{2}tan^{-1}\left(\frac{x - x_{\text{-}}}{z - z_{\text{-}}}\right) + \frac{1}{2}tan^{-1}\left(\frac{x - x_{+}}{z - z_{+}}\right) \tag{4.2}$$

where $(x_{\text{-}}, z_{\text{-}})$ and $(x_{+}, z_{+})$ respectively correspond to the location of the two -1/2 and +1/2 disclination lines. In our simulations, two disclination lines are separated by a distance $d_x$=3.2 units and are located at the same vertical coordinate $x$ along $y$ direction. In this case, the simulation geometry we use is the same as what we use in section 4.1.2. The radius here is 0.2 units.

Figures 4.18 - 4.21 show four different time steps to describe the process for the annihilation of the two disclination lines and how they interact with the topological defects associated with particles. As indicated in Figure 4.18, at the beginning of the simulation, the two-disclination lines in $y-z$ plane are far away from the particle and the director field in the neighborhood of the particle is quasiuniform. There is a Saturn ring generated in the $x-y$ plane. During the annihilation of two disclination lines, gradually they get close

to each other (Figure 4.19). When the two lines interact with the defect that accompanies the particle, the lines are distorted near the particle (Figure 4.20)). At last, as the disclination lines annihilate, the final configuration corresponds to a particle surrounded by a new Saturn ring in the $y - z$ plane (Figure 4.21). The Saturn ring has rotated by 90 degrees (compare Figure 4.18 and 4.21). From this case, we study the effects of one particle on the dynamic behavior of disclination lines. The results from this unsteady simulation compare well with results from another numerical study [9]. This provides confidence in the ability of the present numerical approach for not only obtaining the expected steady state but also for capturing the unsteady dynamics as expected.

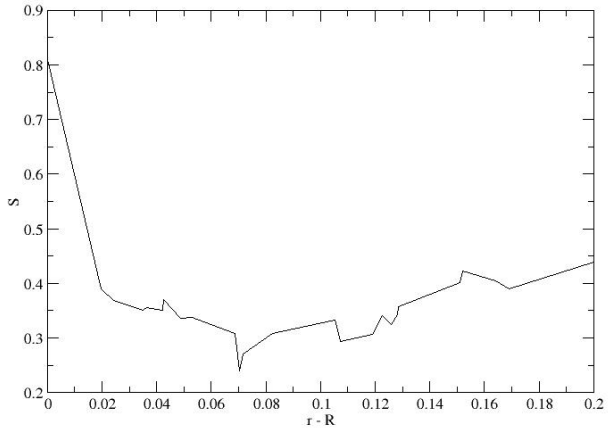


Figure 4.14

Scalar order parameter profile for the ring defect along the direction $\theta$ = $\pi$/2 when $R$ = 0.2 (the ratio $(r - R)/R = 0.35$)

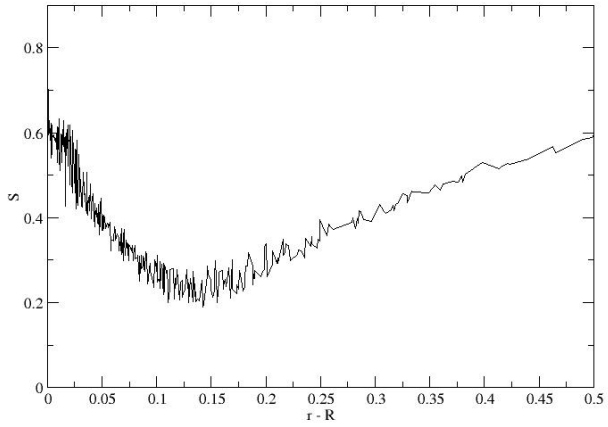


Figure 4.15

Scalar order parameter profile for the ring defect along the direction $\theta$ = $\pi$/2 when $R$ = 0.5 (the ratio $(r - R)/R = 0.30$)

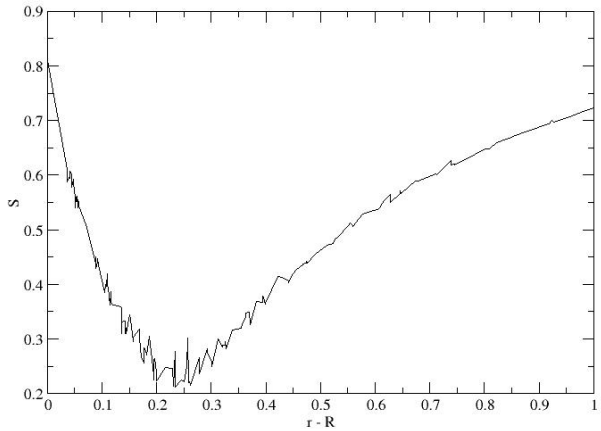


Figure 4.16

Scalar order parameter profile for the ring defect along the direction $\theta$ = $\pi$/2 when $R$ = 1.0 (the ratio $(r - R)/R = 0.25$)

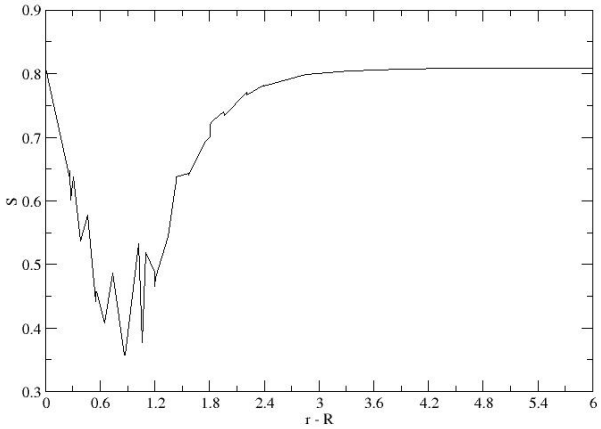


Figure 4.17

Scalar order parameter profile for the ring defect along the direction $\theta = \pi/2$ when $R$ = 6.0 (the ratio $(r - R)/R = 0.15$)

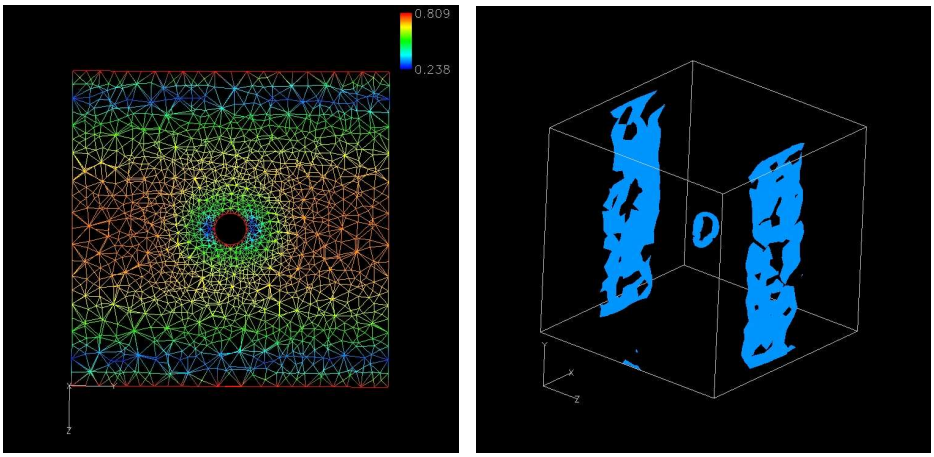


(a) (b)

Figure 4.18

Annihilation of two disclination lines with a particle centered in the cube. $T = 30k$: (a) scalar order parameter in $y - z$ plane with $x = 0$; (b) iso-surface for scalar order parameter where $S = 0.32$

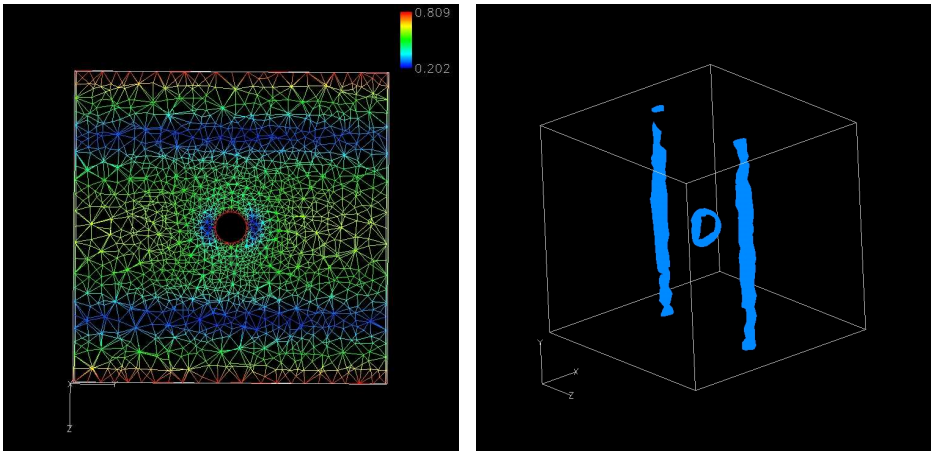


(a) (b)

Figure 4.19

Annihilation of two disclination lines with a particle centered in the cube. $T = 300k$: (a) scalar order parameter in $y - z$ plane with $x = 0$; (b) iso-surface for scalar order parameter where $S = 0.28$

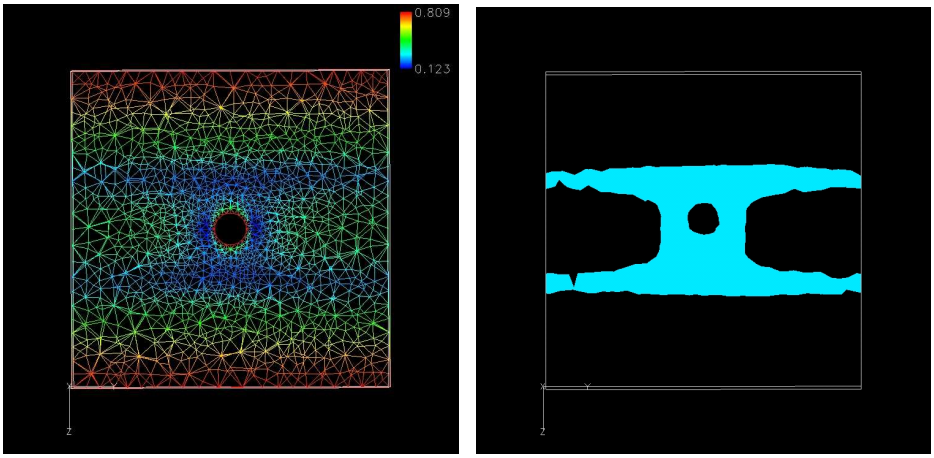


(a) (b)

Figure 4.20

Annihilation of two disclination lines with a particle centered in the cube. $T = 450k$: (a) scalar order parameter in $y - z$ plane with $x = 0$; (b) iso-surface for scalar order parameter where $S = 0.28$

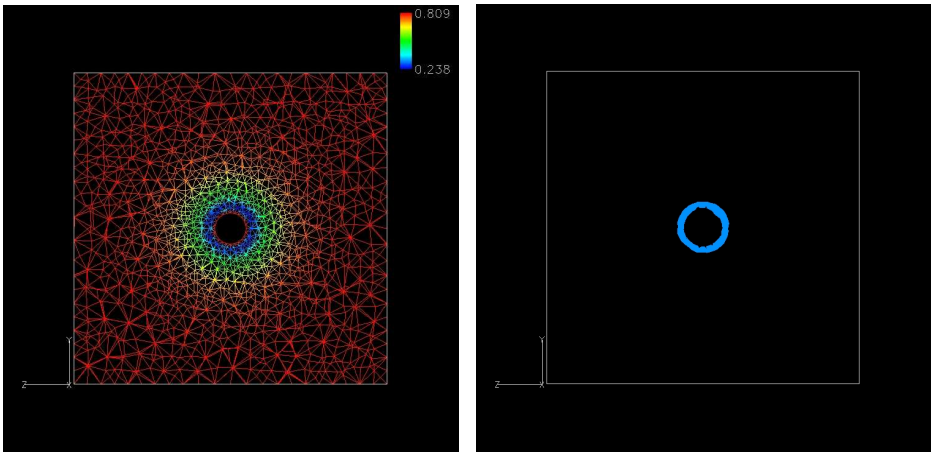


(a) (b)

Figure 4.21

Annihilation of two disclination lines with a particle centered in the cube. $T = 600k$: (a) scalar order parameter in $y - z$ plane with $x = 0$; (b) iso-surface for scalar order parameter where $S = 0.32$

## 4.3 Interaction between spherical colloids

In previous sections, we have studied the defect structure for one spherical particle immersed in LCs, and how one spherical particle interacts with the disclination lines in LCs. In this section, we will study the interactions between spherical particles dispersed in LCs.

### *4.3.1 Two particles at different angles of orientation*

In this case, two spherical particles are located in LCs and different values are chosen for the angle between the director configuration in the far field (along x direction in this case) and the line connecting the centers of the spheres (e.g. 0, 30, 60 and 90 degrees).

The outer boundary corresponds to a cubic domain of length 24 units. The radius of each of the spheres is 3 units and the distance of separation between the centers of the spheres is 10 units which is $5/3^{rd}$ of the diameter. The director is initially aligned along the x direction with $n = (1, 0, 0)$. The chosen mesh contains about 214,000 computational volume elements.

Figures 4.22 - 4.25 show the pattern of streamlines of the director and variations in the order parameter. The preferred orientation in the areas between the spheres is along the line connecting the sphere centers. These are in good agreement with the corresponding results obtained in a study using molecular dynamics simulations [1] (see Figure 4.26).

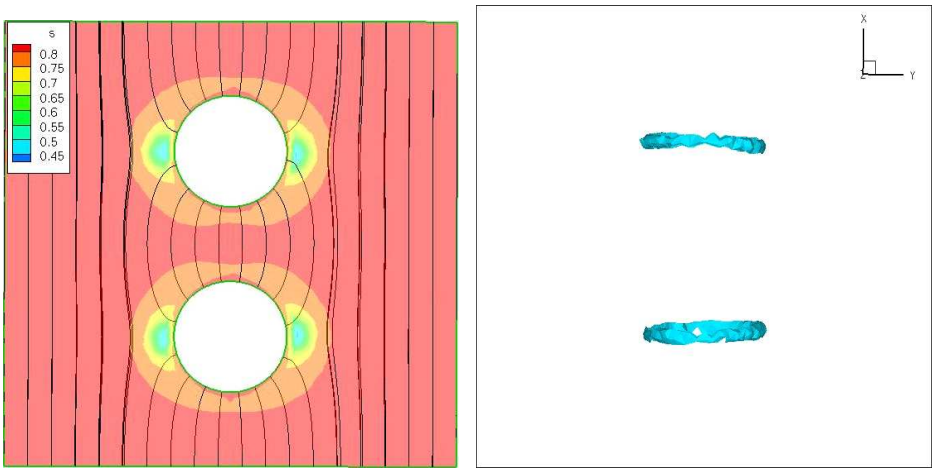


(a) (b)

Figure 4.22

Interaction between spheres with angle = 0 degree: (a) streamline and scalar order parameter; (b) iso-Surface when $S = 0.49$

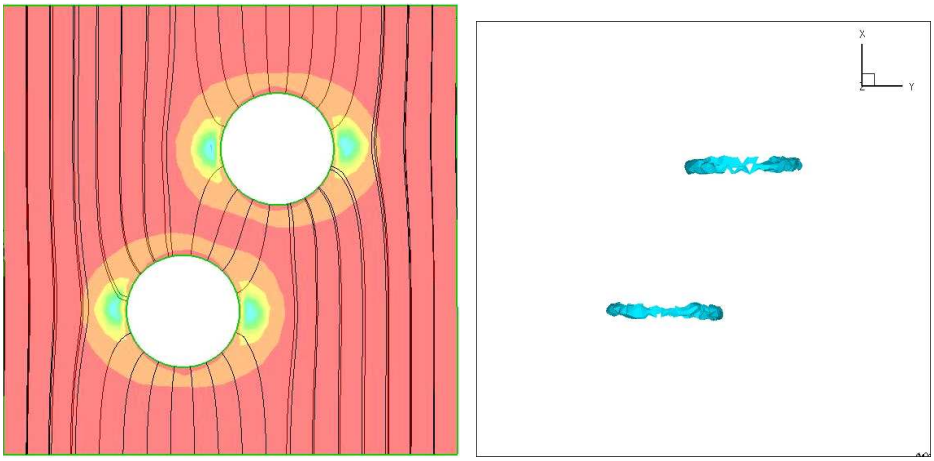

(a) (b)

Figure 4.23

Interaction between spheres with angle = 30 degree: (a) streamline and scalar order parameter; (b) iso-Surface when $S = 0.49$

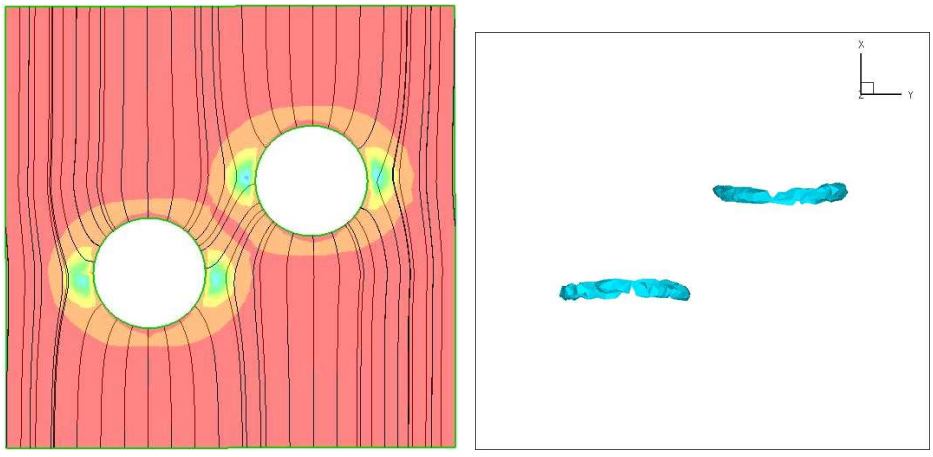

(a) (b)

Figure 4.24

Interaction between spheres with angle = 60 degree: (a) streamline and scalar order parameter; (b) iso-Surface when $S = 0.49$

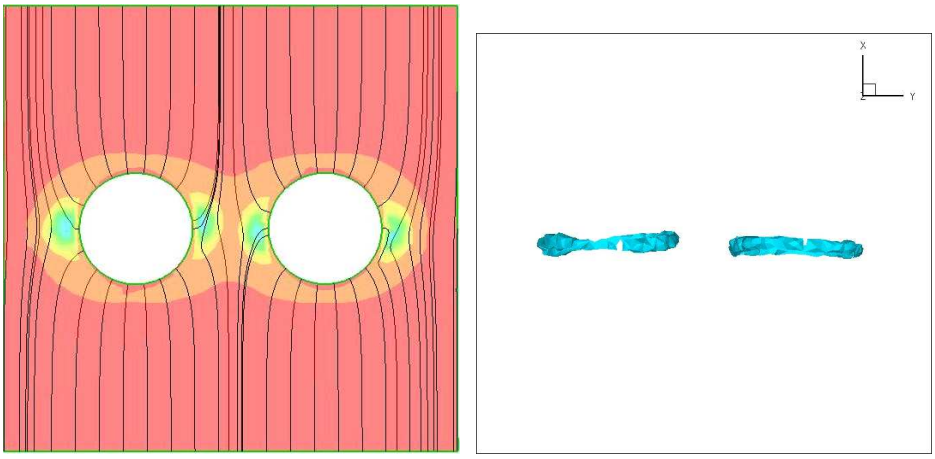

(a) (b)

Figure 4.25

Interaction between spheres with angle = 90 degree: (a) streamline and scalar order parameter; (b) iso-Surface when $S = 0.49$

From the iso-surface images for these cases, it is seen that the distance between these two particles is not small enough to give rise to interaction between the defect patterns of these particles. Such interactions are studied in the next section.

### *4.3.2 Interaction between two spheres*

In this case, two spherical particles are located in the LC with an angle of 90 degrees between the director configuration in the far field and the line connecting the centers of the spheres. The outer boundary corresponds to a cubic domain of length 15 units.

The radius of the spheres is 2.5 units and the distance of separation between the centers of the spheres is 6 units. The director is initially aligned along the $x$ direction with $n = (1, 0, 0)$. The chosen mesh contains 56,771 computational volume elements.

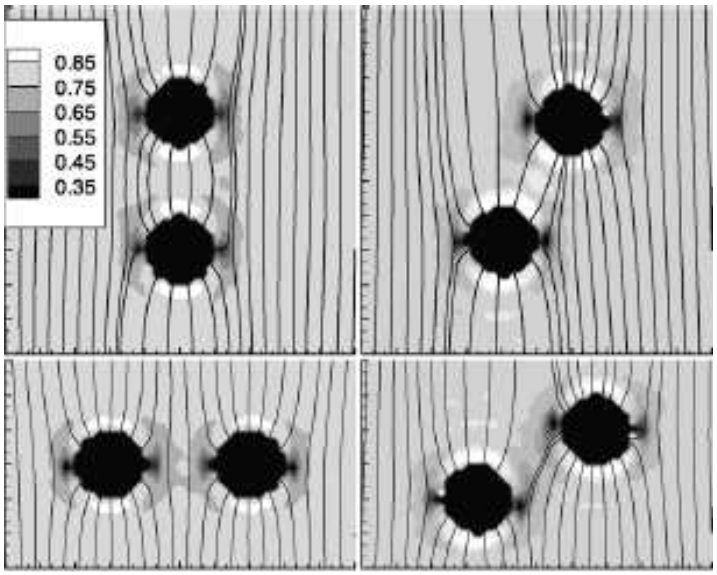


Figure 4.26

Local nematic order parameter S(r) around the macroparticles. The separation is $d = 12B$ with (clockwise from top left) angles $\theta$ = 0 degree, 30 degrees, 60 degrees and 90 degrees. Super-imposed on the map are streamlines of the local director field $n(r)$ (figure reproduced from [1])

Figures 4.27 - 4.31 show the converged solution for this case in terms of iso-surfaces and contour plots for the scalar order parameter and in terms of the director orientation. In this example the Saturn ring defect patterns associated with the two spheres interact with each other and a third ring that is perpendicular to the two Saturn rings around the particles is seen in the solution. The occurrence of this defect structure involving three rings has also been observed in other numerical studies [10, 14]. Reduction in the distance between the particles causes a significant change in the structure of the defects.

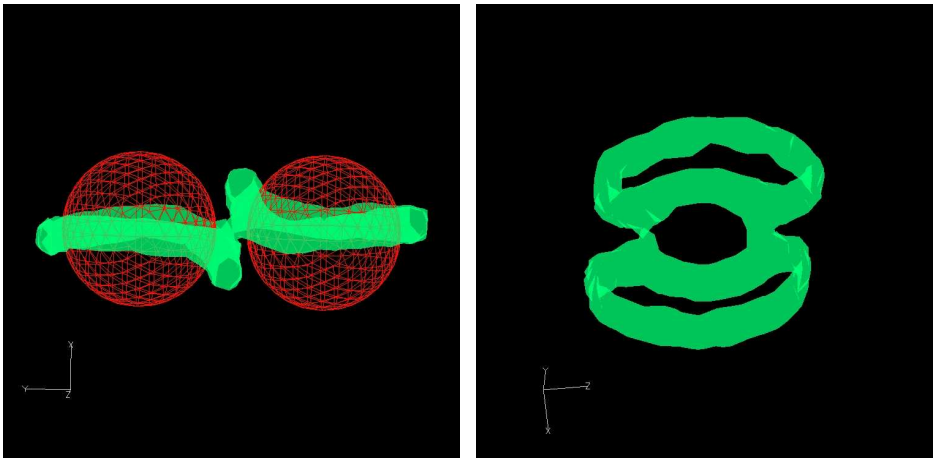

(a) (b)

Figure 4.27

Iso-surface for the scalar order parameter where $S = 0.56$ from two perspectives (a) and (b)

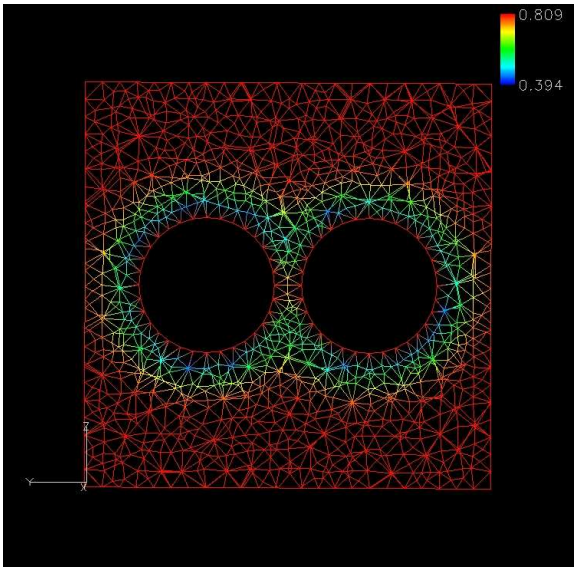


Figure 4.28

Contour maps for scalar order parameter in $y - z$ plane with $x = 0$

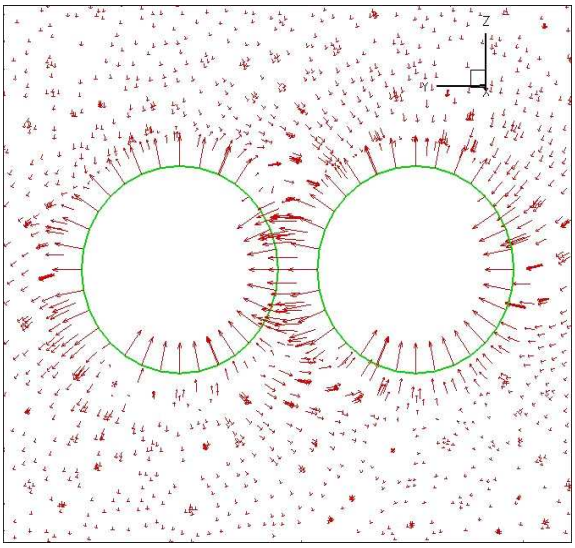

Figure 4.29

Contour maps for director in $y - z$ plane with $x = 0$

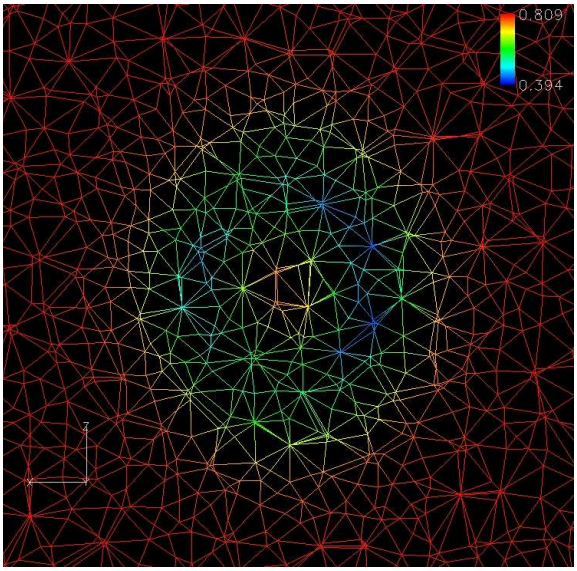


Figure 4.30

Contour maps for scalar order parameter in $x - z$ plane with $y = 0$

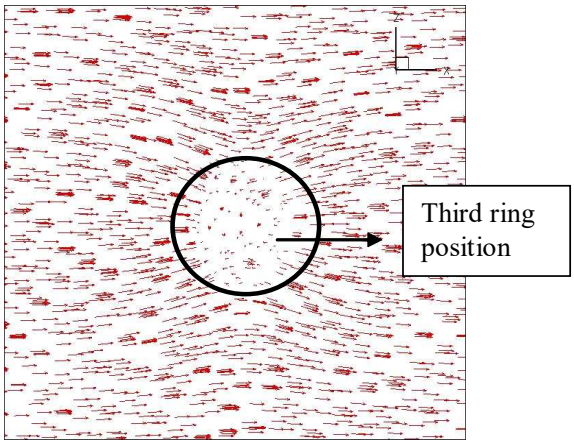


Figure 4.31

Contour maps for director in $x - z$ plane with $y = 0$

### 4.4 Defect structures with the spherical particles adsorbed on substrates

In previous sections, all the cases are studied when the spherical particles are centered in the cubic regions, which are far away from the solid walls. In this section, we will study the defect structure when the particles are adsorbed on the interface boundary between the LC medium and the solid walls. This assists in studying the ligand-receptor binding at the interface boundary and is more suitable for the actual configuration of the sensor. Two point correlation function is used to study the time evolution of dynamics in LCs and the effects of the concentrations of the spheres. Optical pictures are also included.

In this section, two geometries are considered. In the first geometry (Figure 4.32.(a); denoted as 2*2 case later), there are a total of eight spheres with a 2*2 array of spheres in contact with the top solid wall (interface boundary) and another 2*2 array in contact with the bottom solid wall. The radius of each sphere is 2.5 units and the outer boundary corresponds to a cubic domain of length 24 units. The chosen mesh contains 56,771 computational volume elements. In the second geometry (Figure 4.32.(b); denoted as 4*4 case later), there are 32 spheres with one 4*4 array of spheres in contact with the top and bottom solid walls each. The radius is 2.5 units and the outer boundary corresponds to a cubic domain of length 24 units as in the 2*2 case. Thus the 2*2 and 4*4 cases have different concentrations of packing of the spheres at the interface boundaries. The chosen mesh for the 4*4 case contains 662,315 computational volume elements. In the simulations for these two cases the parameter $\epsilon$ (this controls the extent of randomness associated with the director orientation in the initial condition) is chosen as 0.5 ($0 \leq \epsilon \leq 1$,

refer to chapter III). The computation time required to obtain converged solutions was not significantly different for the cases with $\epsilon = 0.5$ and $\epsilon = 0.0$.

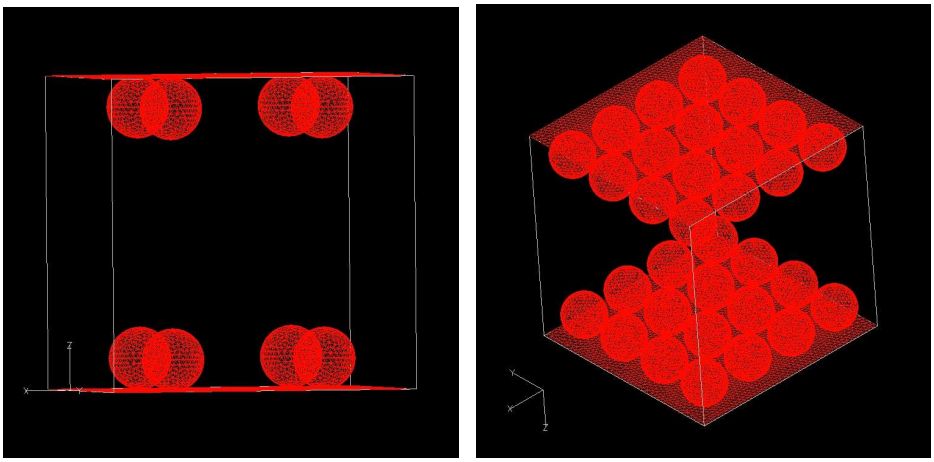

(a) (b)

Figure 4.32

Geometry: (a) 2*2 case; (b) 4*4 case

Figures 4.33 - 4.36 show the variation of the scalar order parameter after convergence to a steady state. Some observations about these solutions are as follows:

- For the 2*2 case, the converged solutions contain disclination lines (regions characterized by abrupt change in orientation) in the form of a Saturn ring surrounding each spherical particle.
- For the 4*4 case, the presence of adsorbed particles causes changes in the order parameter throughout the interface boundaries. Owing to the short distance between the spheres in this geometry, the defect patterns associated with the spheres interact with each other (this topic has been discussed in the previous section).
- The director orientation is quasiuniform (along x-direction) except in the vicinity of the spherical particles, where occurrence of topological defects dominates the solution.

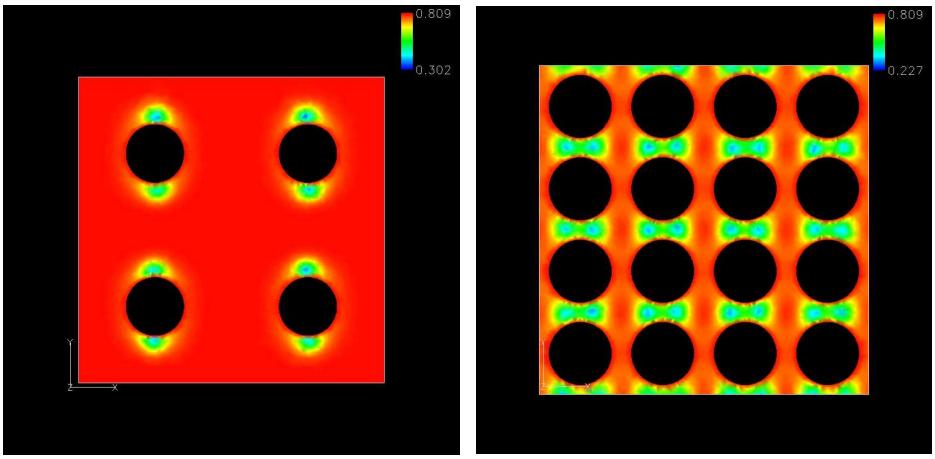


(a) (b)

Figure 4.33

Cut surface for the contour of scalar order parameter in $x-y$ plane passing through the center of the spheres: (a) 2*2 case; (b) 4*4 case

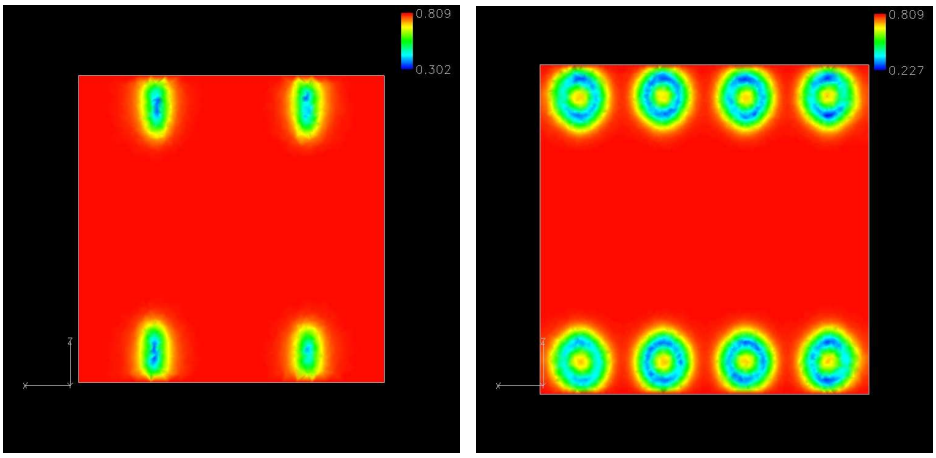


(a) (b)

Figure 4.34

Cut surface for the contour of scalar order parameter in $x-z$ plane: (a) 2*2 case, the cut plane is close to the spheres; (b) 4*4 case, the cut plane is between the pair of spheres

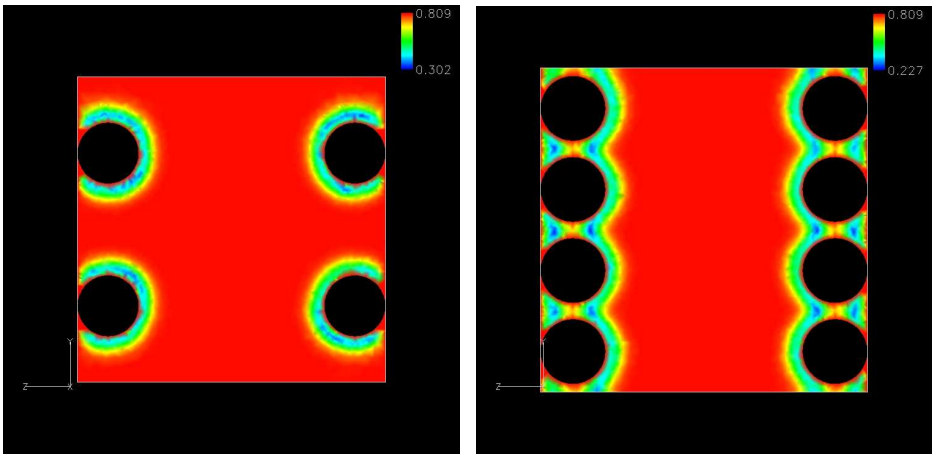


(a) (b)

Figure 4.35

Cut surface for the contour of scalar order parameter in $y-z$ plane passing through the center of the spheres: (a) 2*2 case; (b) 4*4 case

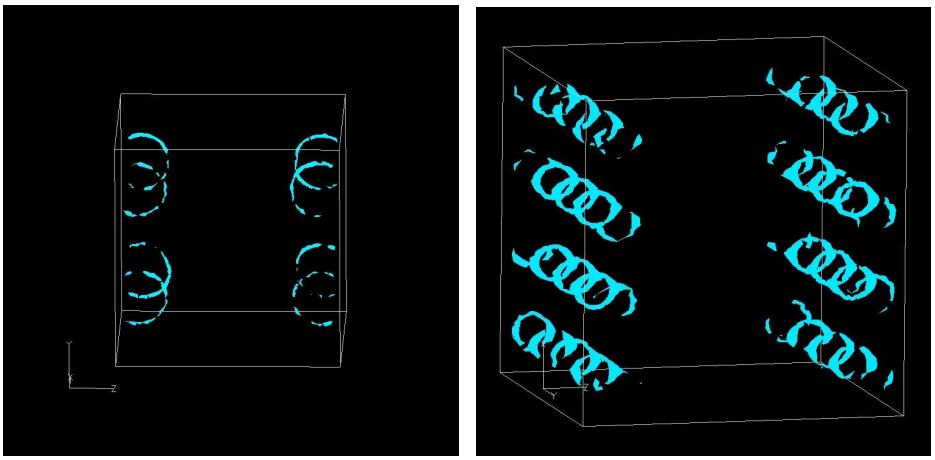

(a) (b)

Figure 4.36

Iso-Surface: (a) 2*2 case with $S = 0.42$; (b) 4*4 case with $S = 0.34$

One way to quantify the overall state of the whole system and its time evolution is through a two point correlation function. This provides an average measure of the extent to which properties at one point in the computational domain are close to the properties at a second point as a function of the distance between the two points. This two-point correlation function is defined as follows:

$$C(x,y,z,t) = \frac{\int_{xmin}^{xmax}\int_{ymin}^{ymax} Tr[Q(x_r+x, y_r+y, z, t)Q(x_r, y_r, z, t)]dy_r dx_r}{\int_{xmin}^{xmax}\int_{ymin}^{ymax} Tr[Q(x_r, y_r, z, t)]^2 dy_r dx_r}$$

Figures 4.37 - 4.39 show the evolution of the correlation function $c(x, y, z)$ at different times for the 2*2 case. To provide an idea about the variation of this function in space at steady state, plots have been included for cut section at different regions. From these images, we can observe the following:

- When t = 0 (initial condition, see Figure 4.37), we see that the value of the correlation function is low everywhere, which means director is not uniform. This is because the chosen initial condition does not correspond to uniform orientation. But as we have mentioned before, it is not a completely random initial condition, and there is still some correlation between properties at different points. For a complete random initial condition ($e = 1$), the value for the correlation function should be close to zero everywhere.
- For $t = 5000$ steps (Figure 4.38), the value of the correlation function increases and this suggests that there is a tendency for the director orientation at different regions to approach the preferred orientation in the far field.
- Finally, when the system is in steady state (Figure 4.39), we can find the value of correlation function is close to one in some regions (4.39.(d)) and is low in other regions (Figure 4.39 (b) & (c) ). It means that the surfaces impose a quasi uniform nematic order in the whole domain, which is slightly perturbed by the presence of a few topological defects attached to the particles.

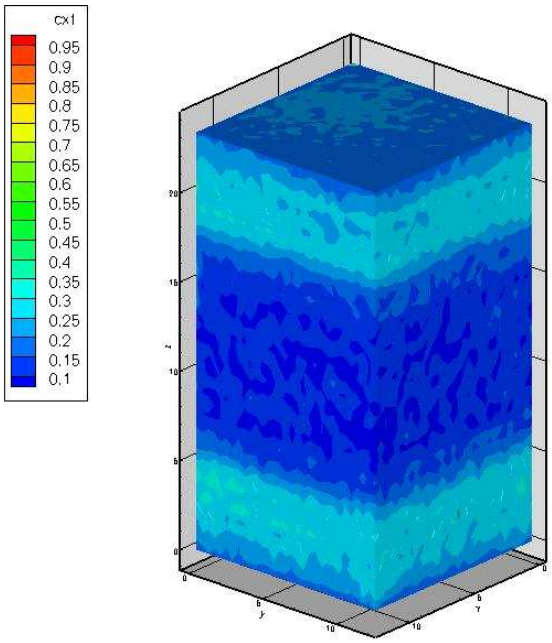


Figure 4.37

Contour map for correlation function $c(x, y, z)$ for 2*2 case when $t = 0$ computational time step

Note that as a consequence of the use of periodic boundary conditions in $x$ and $y$ directions, the correlation function in these directions is defined in a range corresponding to half the length of the physical domain in these directions (i.e. for 12 units of length instead of 24 units of length).

The time evolution for the 4*4 case is similar to that obtained for the 2*2 case discussed above. To study the effects of concentration of spheres, we can compare the correlation function obtained for the 4*4 case at steady state (Figure 4.40) with corresponding results for the 2*2 case (Figure 4.39).

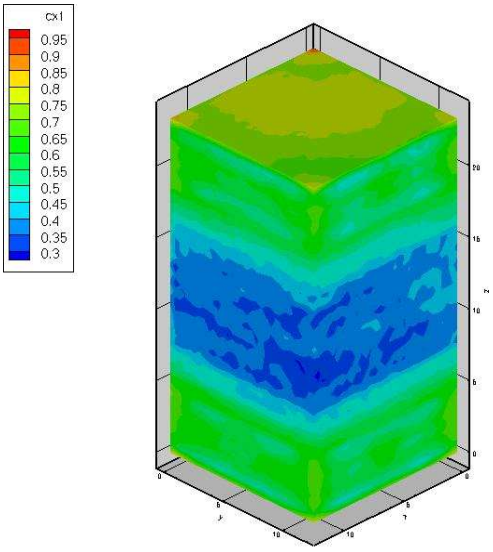


Figure 4.38

Contour map for correlation function $c(x, y, z)$ for 2*2 case when $t = 5,000$ computational time steps

For both the cases, except at regions close to the spheres, the director orientation is close to the orientation in the far field. In the regions close to the spheres, the value for correlation function is lower in 4*4 case than in 2*2 case. This shows that as the concentration of particles increases, the nematic order is perturbed more by the presence of topological defects. At a critical concentration, no long-range uniform nematic order is observed [7]. A systematic study of the behavior of the sensor at several concentrations of the analyte is a topic of interest in future studies.

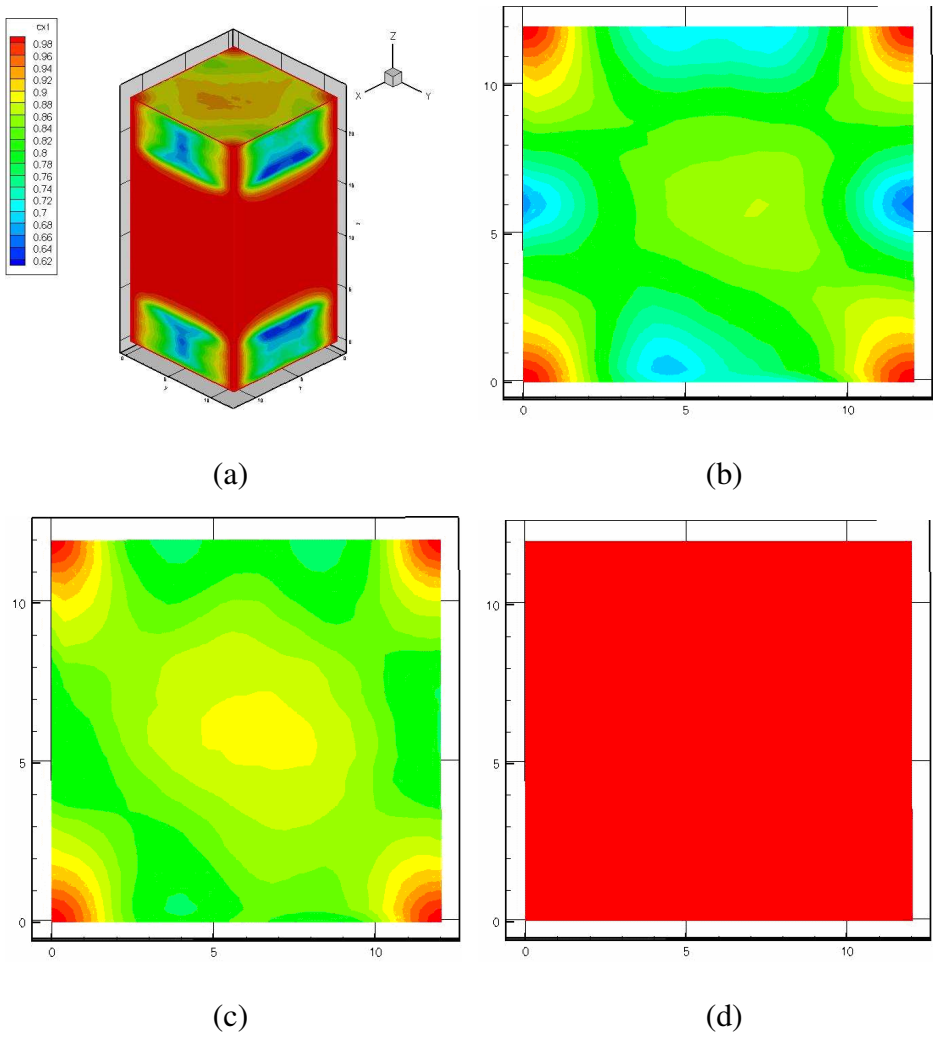


Figure 4.39

Correlation function for 2*2 case when $t = 1000,000$ computational time steps: (a) $c(x, y, z)$ in the whole domain; (b) a cut plane section in $x - y$ plane of (a) passing through the center of the spheres; (c) a cut section in $x - y$ plane of (a) for the areas touching the spheres; (d) a cut section in $x - y$ plane of (a) in the center of the cube

Note that Figure 4.40.(c) shows some periodic pattern in $x$ and $y$ direction for two point correlation function. This is because of the special arrangement for the array of spheres (the radius of the spheres, the distance between the pair of spheres are all same), in which each of spheres can be viewed with the periodic boundary condition in $x$ and $y$ direction.

Figure 4.41 shows a plot of the optical pictures (obtained by plotting the quantity $(n_x n_y)^2$ where $n_x$ and $n_y$ are $x$ and $y$ component of the local director) for the 2*2 and 4*4 cases. This quantity is related to the intensity of light passing through the sensor. The optical pictures indicate a quasi long-range uniform order perturbed to different extents by the topological defects attached to the particles in these two cases.

## 4.5 Defect structure for one biological macromolecule

Till this stage the substances present within the LC medium in the sensor have been modeled as spherical particles. In this section, we focus on the development for a framework that can handle cases involving complex three-dimensional geometries with particular emphasis on modeling the presence of biological macromolecules.

### *4.5.1 Generation of the geometry for macromolecule*

In this work, based on the relevance for clinical applications of biosensors, Immunoglobulin G (IgG, a protein that acts as an antibody), has been selected as the sample biological macromolecule. The stages in the construction of the surface mesh to represent IgG are illustrated in Figure 4.42. Firstly, the PDB (protein data bank) file for human Immunoglobulin G was chosen (Figure 4.42.(a)).

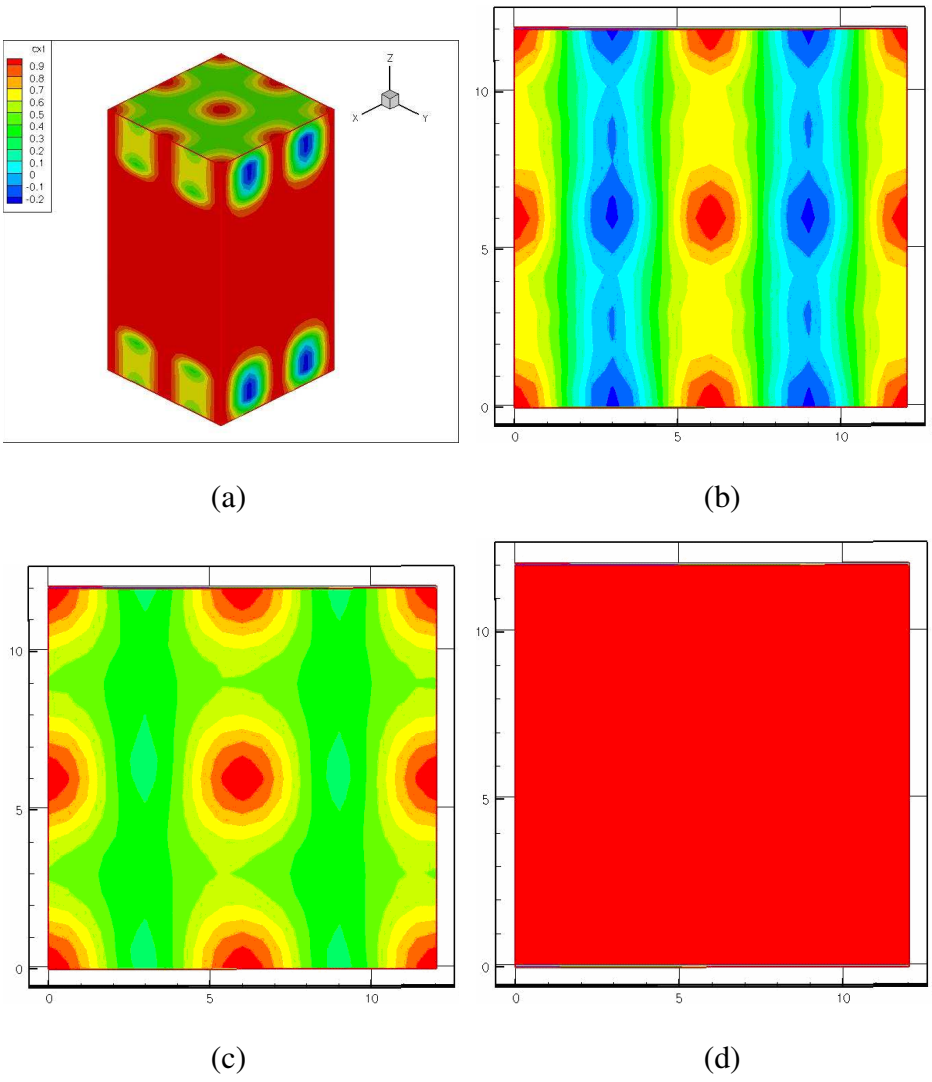


Figure 4.40

Correlation function for 4*4 case when $t = 400,000$ computational time steps: (a) $c(x, y, z)$ in the whole domain; (b) a cut plane in $x - y$ plane from (a) passing through the center of the spheres; (c) a cut plane in $x - y$ plane from (a) touching the spheres; (d) a cut plane in $x - y$ plane from (a) passing through the center of the cube

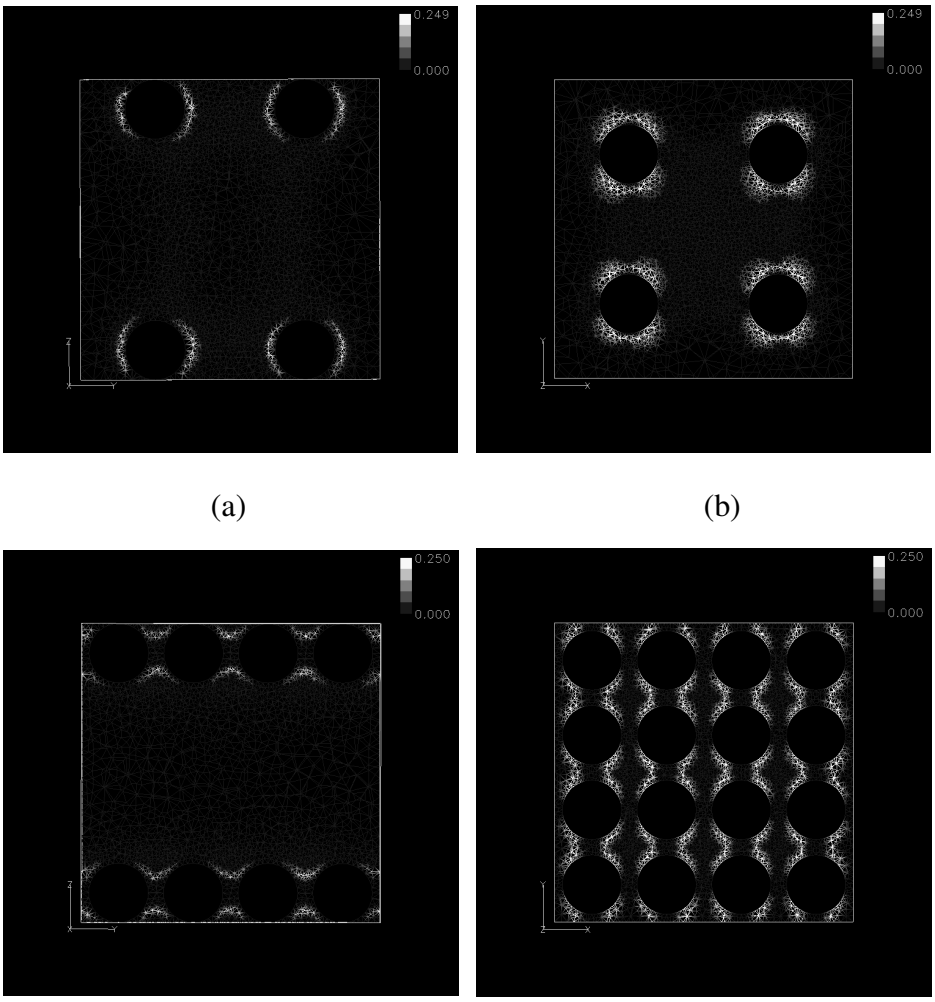


Figure 4.41

Nematic ordering in the presence of particles adsorbed at the interface boundaries: optical picture in steady state. Cut surface passing through the center of the spheres. (a) 2*2 case in $y-z$ plane; (b) 2*2 case in $x-y$ plane; (c) 4*4 case in $y-z$ plane; (d) 4*4 case in $x-y$ plane

Secondly, a preliminary surface mesh with triangular faces was constructed [23] (Figure 4.42.(b)). Thirdly, remeshing of the surface mesh (Figure 4.42.(c)) was performed to eliminate regions characterized by significantly higher resolution compared to the average resolution in adjacent regions [27]. Finally, Laplacian algorithm was used to smooth the surface mesh (Figure 4.42.(d)). The surface mesh created was used as an internal boundary for the construction of a volume mesh that represents the physical region occupied by the liquid crystal medium surrounding the macromolecule. Figure 4.43. shows a cut-section of the volume mesh in the vicinity of the IgG and illustrates the variation in resolution used (high resolution close to the IgG, low resolution in the far field region). The state of the liquid crystal is computed in the volume mesh. The length of the cubic domain is 3.2 units and the number of computational cells is about 785,000 computational elements. The coordinates in the PDB file are in Angstrom units and the reference length for the present study is taken as 20nm or 200 Angstrom. Hence the coordinates from the PDB file have been scaled by a factor of 200 (1/200).

### *4.5.2 The defect structure for one IgG at the center of cube*

Fig. 4.44 shows the defect structure for one IgG macromolecule in the center of the cubic domain through plots for iso-surface, scalar order parameter and biaxiality parameter. From these images, we can observe that there is a defect structure around the macromolecule, (this represents a sudden change in the orientation of the director) characterized by a low value for the scalar order parameter and a high value for biaxiality parameter.

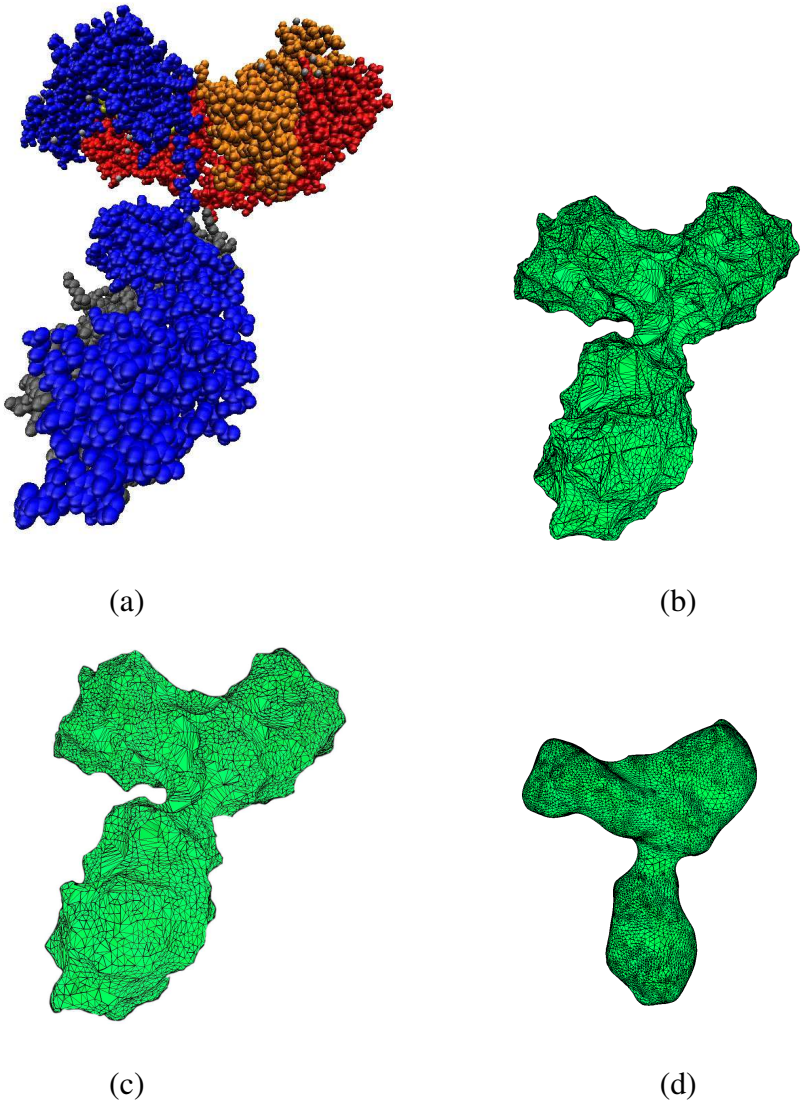

(a) (b)

(c) (d)

Figure 4.42

Construction of an unstructured mesh to represent a biological macromolecule. The sequence of successive stages is shown in (a) to (d)

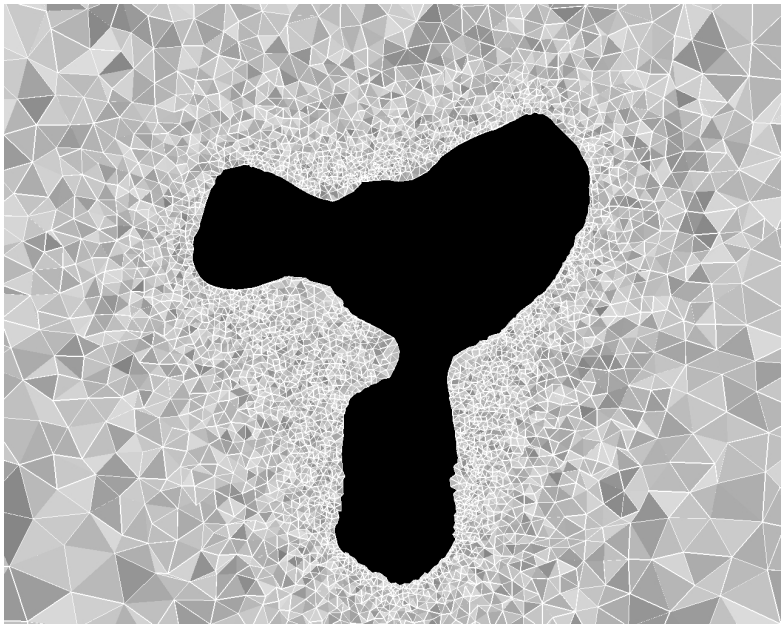

Figure 4.43

Cut section of volume mesh

The defect is close to the IgG structure and in a plane perpendicular to the far-field-director. In the far-field, the director is uniform and along the preferred orientation (x-axis). It shares the similarity in this aspect with the Saturn ring configuration for the case with a spherical particle (Saturn ring configuration is stable in a plane perpendicular to the far-field-director).

Instead of specifying the far-field director orientation along the x direction (case shown in Fig. 4.44), it is specified along the y direction in the next case. Unlike the case involving a spherical particle, due to the lack of symmetry for the IgG macromolecule, significant changes in the defect structure can occur when a change in the far field director orientation is imposed.

Figure 4.45 shows an iso-surface for the scalar order parameter when the far-field director orientation is along y-axis. Note that in Figure 4.45, the defect structure is not predominantly confined to a plane perpendicular to the far field orientation and is closely influenced by the IgG geometry. A complex defect structure is observed. This case underscores the importance of using three-dimensional simulations to study the defect structure for cases with complex geometry. For this case, use of a two-dimensional simulation can not provide a good description of the defect structure.

To verify that the resolution used in performing the above simulations for IgG was adequate, another volume mesh with higher resolution (1,396,795 computational elements, see Figure 4.43) was used and the computation corresponding to results shown in Figure 4.44 were repeated. Comparison of Figure 4.44.(a) with the corresponding results for the case with higher resolution (see Figure 4.47) shows approximately the same results. Based on this comparison we can conclude that the resolution chosen previously is adequate.

### *4.5.3 The defect structure for one IgG adsorbed on substrates*

Now we consider modeling the presence of IgG at the interface boundary, a case of more practical interest for studying the sensor configuration. The effect of an adsorbed biological macromolecule at an interface and its influence on the liquid crystal medium can be studied.

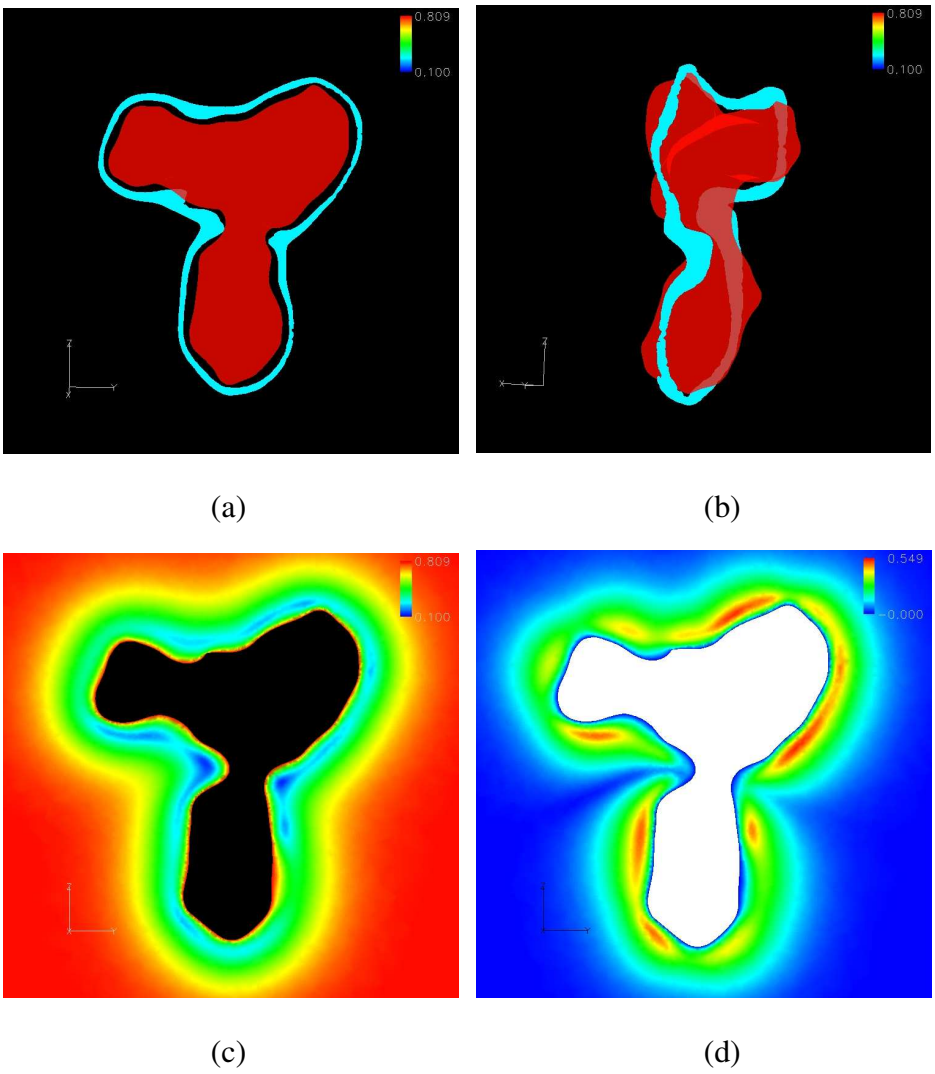


(a) (b)

(c) (d)

Figure 4.44

Defect structure around one antibody IgG in the center of the cubic domain with far-field director along x-axis: (a) iso-surface of the scalar order parameter where $S = 0.27$; (b) different view of case shown in (a); (c) scalar order parameter map in $y - z$ plane with $x = 0$; (d) biaxiality parameter map in $y - z$ plane with $x = 0$

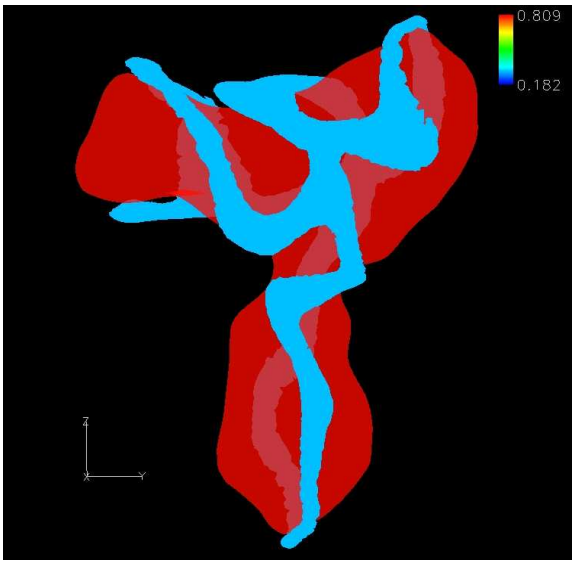


Figure 4.45

Defect structure around one antibody IgG in the center of the cube with far-field director along y-axis. Iso-surface for scalar order parameter where $S = 0.3$

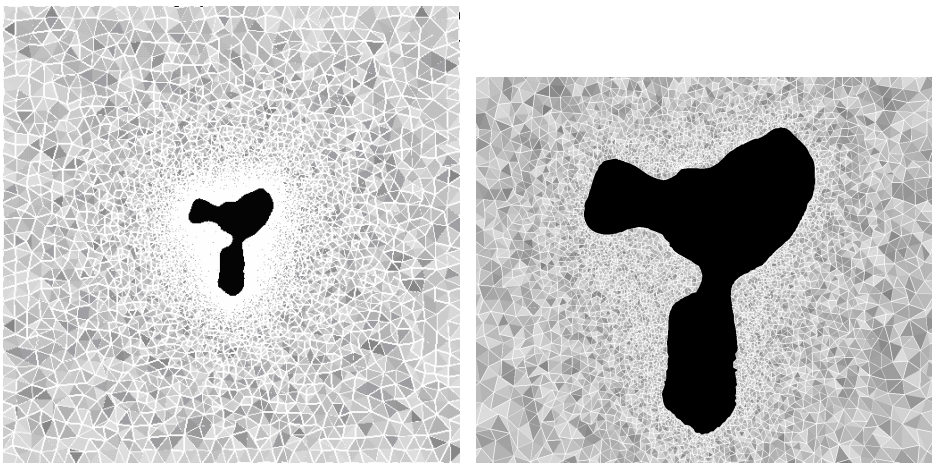

(a) (b)

Figure 4.46

Cut section of high resolution volume mesh showing the faces of the tetrahedral elements of the volume mesh. (b) is a magnified view of the region close to the particle

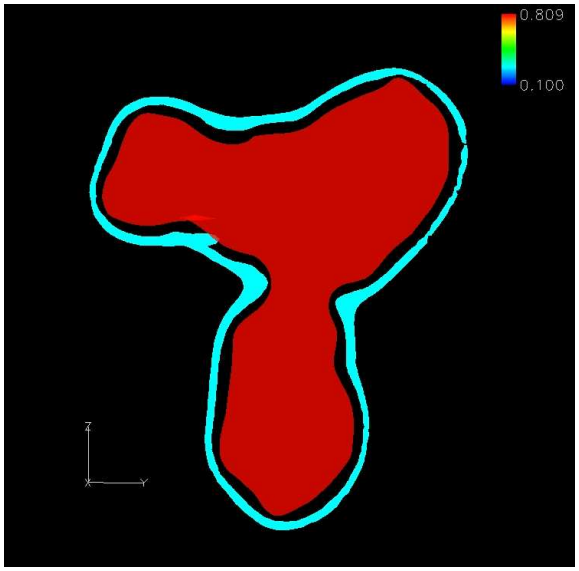


Figure 4.47

Defect structure around one antibody IgG in the center of the cube with far-field director along x-axis with high resolution volume elements. Iso-surface for scalar order parameter where $S = 0.27$

The antibody IgG can be roughly considered as a Y-shaped object with two Fab (antigen-binding) fragments corresponding to the left and right segments at the top and one Fc (constant) fragment on the bottom (see Figure 4.43). Results from a theoretical study [27] and a related experimental study [26] suggest that a high positive charge distribution at the interface will favor an 'end-on' orientation of IgG at the interface (Fc fragment is close to the interface and Fab fragments are far from the interface). The end-on orientation is the preferred choice in applications involving immunoassays with IgG. The 'head-on' orientation (Fc fragment is far from the interface and Fab fragments are close to the surface) is not the preferred orientation.

In this work, we study the cases involving the antibody IgG adsorbed at the interface boundary with both 'end-on' and 'head-on' orientations. The results are shown in figures 4.48 - 4.49. It helps us to study the optical behavior of the sensor for cases involving preferred and non-preferred orientations. There are about 820,000 computational elements. The far-field orientation is along the x-axis (Figure 4.48) or y-axis (Figure 4.49).

Figure 4.50 shows the defect structure for a case involving the antibody IgG adsorbed on a curved wall with 'end-on' orientations. Use of a non planar boundary surface enables accounting for effects associated with nanoscale topography at the interface in simulation of this LC based sensor.

The present case only considers one IgG macromolecule, but the same method can be used for a case involving several macromolecules. From the detailed solution for the state of liquid crystal system, an estimate for the intensity of light transmitted through the liquid

crystal film can be obtained in terms of a function of variables [7] (e.g. the concentration of the particles adsorbed at the substrate) and this can be compared with the experimental results.

Modeling the behavior of a sensor in the presence of a biological macromolecule has been demonstrated using the present framework. Such capabilities enable the developed framework to be used in assisting the design and development of the class of sensors studied in this work.

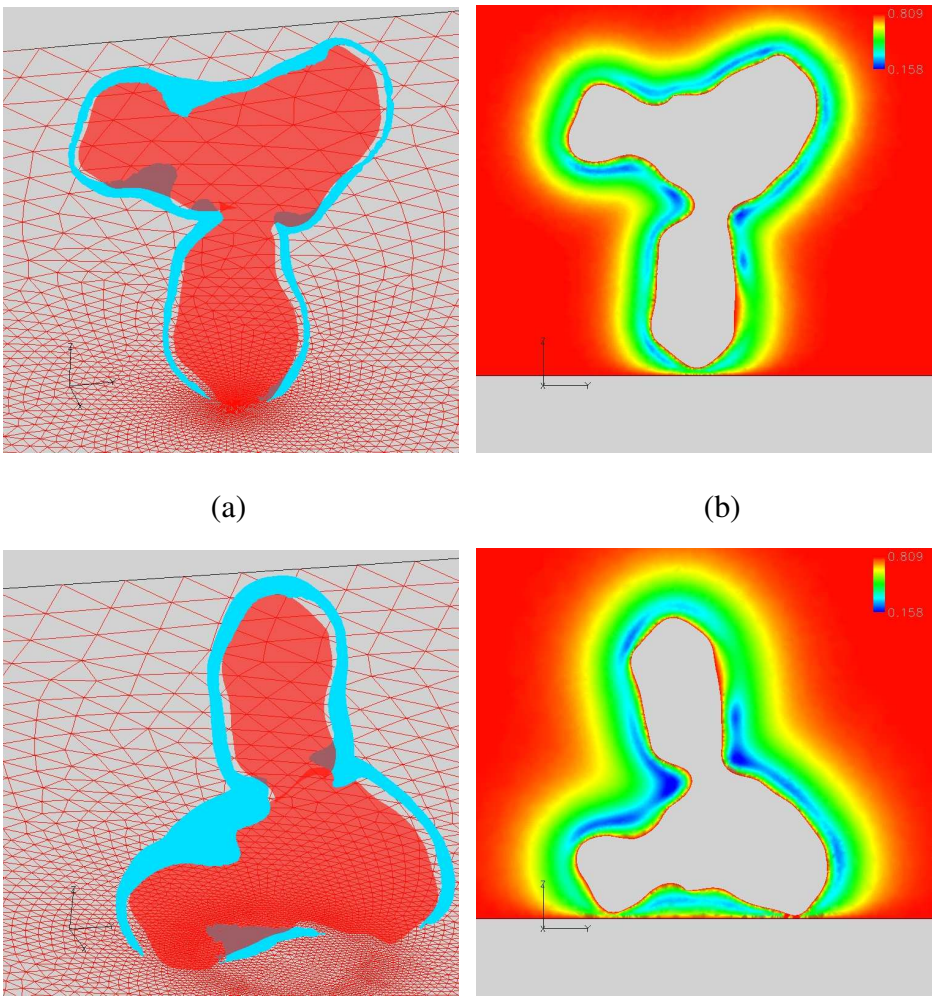


(a) (b)

(c) (d)

Figure 4.48

The defect structure around one antibody IgG adsorbed at the interface boundary with far-field director along x-axis: (a) iso-surface for 'end-on' orientation where $S = 0.3$; (b) scalar order parameter for 'end-on' orientation in $y - z$ plane with $x = 0$; (c) iso-surface for 'head-on' orientation where $S = 0.3$; (d) scalar order parameter for 'head-on' orientation in $y - z$ plane with $x = 0$

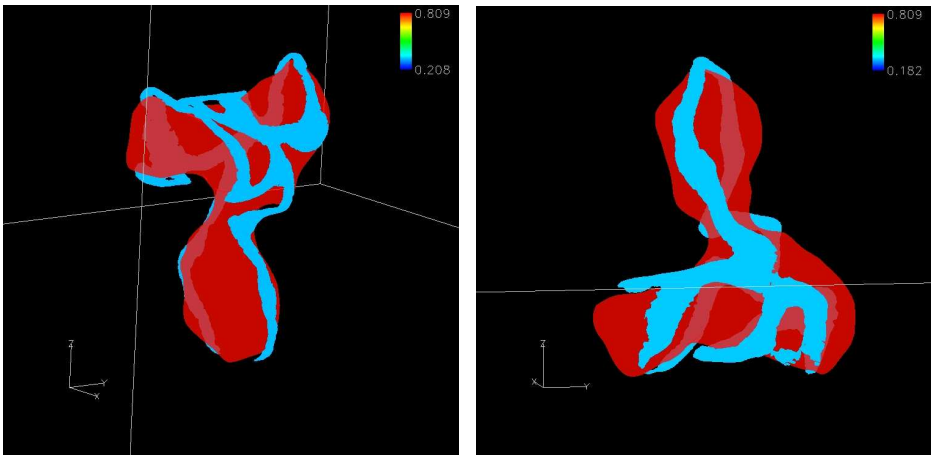


(a) (b)

Figure 4.49

Defect structure around one antibody IgG adsorbed at the interface boundary with far-field director along y-axis: (a) iso-surface for 'end-on' orientation where $S = 0.3$; (b) iso-surface for 'head-on' orientation where $S = 0.3$


Figure 4.50

Defect structure around one antibody IgG adsorbed at the curved substrate with far-field director along x-axis. Iso-surface for 'end-on' orientation where $S = 0.3$

# CHAPTER V

# SUMMARY AND FUTURE WORK

From this work, a simulation framework that uses coarse-grained method with tensor order parameter based on a dynamic field theory for modeling the behavior of a class of liquid crystal based sensors has been studied. Simulations corresponding to the geometries using three-dimensional unstructured meshes have been performed based on solution of an unsteady partial differential equation. Two kinds of shapes of geometries are used in this work. At first, the particles are simply modeled as spheres representing nanoparticles. Then Immunoglobulin $G(IgG)$ has been chosen as a sample case to demonstrate modeling the state of LCs by including a detailed description of the geometry of substances contained within the liquid crystal medium. Through comparisons with results from detailed molecular dynamics based studies in the literature it has been shown that simulations in the present study yield expected trends for orientation of the liquid crystal and its dynamic behavior. Several examples have been chosen for studying the dynamics of liquid crystals in the presence of spherical particles or a biological macromolecule. We have investigated the defect structure for one sphere, the interaction between two spheres and between one sphere and two disclination lines, the dynamics and time evolution for spheres adsorbed on solid surfaces, and the defect structure for a biological macromolecule. From the study

of these cases, we have a good understanding for the defect structure in liquid crystals in the presence of nanoparticles and biological macromolecules. In addition, comparing and contrasting the defect structure associated with different geometries (e.g. spheres, $IgG$) and boundary conditions can help us to obtain insight and to better guide us in the design of suitable biosensors. This study also shows that using three-dimensional simulations can allow us to better understand the defect structure compared with using two-dimensional simulations.

Finally, some suggestions are made regarding future research topics in this area. It remains to be seen whether it is possible to demonstrate that a satellite defect is a stable configuration for large particle size (around 720 nm radius). Extending the scope of the present study to include more than one biological macromolecule, the interactions between the macromolecules and modeling the interface boundary using non planar, wavy walls are of interest. Currently, parameters representative of the liquid crystal 5CB has been used. We may consider other choices for design of this class of liquid crystal biosensors. Use of three-dimensional simulations for estimating the critical concentration of the spherical particles, above which no long-range uniform nematic order is observed, is also of interest.

# REFERENCES


[1] M. P. Allen, ," *Computer Physics Communications*, 2005.

[2] D. Andrienko, G. Germano, and M. P. Allen, ," *Phys. Rev. E*, 2001.

[3] A. N. Beris and B. J. Edwards, *Thermodynamics of Flowing Systems: With Internal Microstructure*, Oxford University Press, New York, 1994.

[4] P. J. Collings, *Liquid Crystals Second Edition*.

[5] P. G. de Gennes and J. Prost, *The Physics of Liquid Crystals, 2nd ed*, Clarendon Press, Oxford, 1993.

[6] J. Fukuda and H. Yokoyama, ," *Eur. Phys. J.*, 2001.

[7] S. Grollau, O. Guzman, N. L. Abbott, and J. J. de Pablo, ," *Chem. Phys.*, 2005.

[8] S. Grollau, E. B. Kim, N. L. Abbott, and J. J. de Pablo, ," *Phys. Rev. E*, 2003.

[9] S. Grollau, E. B. Kim, O. Guzman, N. L. Abbott, and J. J. de Pablo, ," *Phys. Rev.*, 2003.

[10] S. Grollau, E. B. Kim, N. L. A. O. Guzman, and J. J. de Pablo, ," *The Journal of Chem. Phys.*

[11] Y. Gu and N. L. Abbott, ," *Phys. Rev. Lett*, 2000.

[12] V. K. Gupta, J. J. Skaife, T. B. Dubrovsky, and N. L. Abbott, ," *Science*, 1998.

[13] O. Guzman, N. L. Abbott, and J. J. de Pablo, ," *J. Chem. Phys.*, 2005.

[14] E. B. Kim, O. Guzman, S. Grollau, N. L. Abbott, and J. J. de Pablo, ," *J. Chem. Phys.*, 2002.

[15] O. V. Kuksenok, R. W. Ruhwandl, S. V. Shiyanovskii, and E. M. Terentjev, ," *Phys. Rev. E*, 1996.

[16] X. l. Wu, W. I. Goldburg, M. X. Liu, and J. Z. Xue, ," *Phys. Rev. Lett.*, 1992.

[17] E. A. Luke and T. George, "Loci: a Rule-based Framework for Parallel Multi-disciplinary Simulation Synthesis," *Journal of Functional Programming*, 2005.

[18] O. Mondain-Monval, J. C. Dedieu, T. Gulik-Krzywicki, and P. Poulin, ," *Eur. Phys. J.B*, 1999.

[19] N. Mottram, *Introduction to Q-tensor theory*, Department of Mathematics, University of Strathclyde.

[20] P. Poulin, V. A. Raghunathan, P. Richetti, and D. Roux, ," *Journal Phys II*, 1994.

[21] R. W. Ruhwandl and E. M. Terentjev, ," *Phys. Rev. E*, 1997.

[22] O. G. N. L. A. S. Grollau, E. B. Kim and J. J. de Pablo, ," *Phys.*, 2003.

[23] M. F. Sanner and A. J. Olson, ," *Biopolymers*, 1996.

[24] M. Tasinkevych, N. M. Silvestre, P. Patricio, and M. M. T. da Gama, ," *Eur. Phys.*, 2002.

[25] E. M. Terentjev, ," *Phys. Rev. E*, 1995.

[26] H. Wang, D. Castner, B. D. Ratner, and S. Jiang, ," *Langmuir*, 2004.

[27] J. Zhou, H.-K. Tsao, Y.-J. Sheng, and S. Jiang, ," *Chem. Phys.*, 2004.